Effect of drying temperature on the properties of alkali-activated binders - Recommendations for sample preconditioning

Vincent Trincal, Virginie Benavent, Hugo Lahalle, Bastien Balsamo, Gabriel Samson, Cédric Patapy, Yoann Jainin, Martin Cyr

Effect of drying temperature on the properties of alkali-activated binders - Recommendations for sample preconditioning

Vincent TRINCAL[1*], Virginie BENAVENT[1], Hugo LAHALLE[1], Bastien BALSAMO[1], Gabriel SAMSON[1], Cédric PATAPY[1], Yoann JAININ[2], Martin CYR[1]

[1]LMDC, INSAT/UPS Génie Civil, 135 Avenue de Rangueil, 31077 Toulouse cedex 04 France.

[2]Ecocem Materials, 4 Place Louis Armand, 75012 Paris, France.

[*]Corresponding author: vincenttrincal @ gmail.com

Abstract

Various durability tests require a drying step to remove free water without altering the chemistry or microstructure of the materials. However, little is known about the effects of drying on alkali-activated materials (AAMs). This study focusses on the drying stage to assess the behaviour of four alkali-activated binders compared with conventional binders: a metakaolin-based geopolymer, ground granulated blast-furnace slag (GGBS) activated by sodium silicate or by sodium carbonate, and a mixture of metakaolin-GGBS activated by sodium silicate. After a 28-day autogenous cure, mortar and paste samples were dried at temperatures ranging between 20°C and 125°C. Micro-structural damage was observed in metakaolin-based AAMs dried at temperatures above 40°C, but occurred only between 40 and 60°C for GGBS-based AAM. SEM observations and MIP porosimetry coupled with mineralogical analyses, allowed AAMs drying mechanisms to be better understood, and recommendations to be made for the preconditioning of these materials.

Keywords

Alkali-activated binder, Geopolymer, GGBS, Metakaolin, Drying conditions, Preconditioning

1. Introduction

Alkali-activated binders are produced from a source of aluminosilicates (precursor) mixed with a highly alkaline solution (most of the time either sodium (Na) or potassium (K) silicate solutions, but sometimes hydroxide, carbonate or lithium alkali solutions) called the activating solution [1,2]. There are two main types of alkali-activated binders, differentiated by their precursors' calcium contents, the chemical mechanisms that take place upon hydration and eventually the reaction products. For precursors with low calcium content, such as metakaolins and type F fly ashes, the term geopolymer is used [1]. The chemical reactions contribute to a dissolution/polycondensation process, leading to a 3D-aluminosilicate network [3]. For precursors rich in calcium, such as ground granulated blast-furnace slag (GGBS), the reaction process consists of dissolution/precipitation reactions. The main reaction products are C(-A)-S-H type phases ($CaO\text{-}Al_2O_3\text{-}SiO_2\text{-}H_2O$) [4].

Abundant literature is available regarding AAMs formulation, but only a few studies deal with their durability (see reviews by [5–9]). Until recently, to test the durability of AAM matrices, protocols defined for "conventional" binders have often been used, without focusing on protocol impact (in particular of pre-conditioning or drying on the binder structure) or analyses representativeness [10,11]. However, appropriate preconditioning procedures must be selected to avoid potentially misleading conclusions regarding general indicators as well as long-term in-service performance [10–12]. Tests proposed in the literature (see, for example, RILEM framework publications [13,14]) usually require a preconditioning of the specimens, especially a drying step at temperatures ranging from 45°C (e.g. accelerated carbonation XP-P-18-458, 2008), to 80°C (e.g. gas permeability XP-P-18-463, 2011), or even to 105°C (e.g. porosity NF-P-18-459, 2010). Associated with temperature, the relative

humidity can also be fixed for sample preconditioning, e.g. at 57 ± 3% (SIA 262-1, 2013) and higher than 95% (NF EN 12390-2, 2019). Testing procedures should be reviewed considering the chemical and microstructural properties of the AAM, in order to separate microstructural changes caused by preconditioning (drying) from inherent characteristics (properties and specific microstructural development mechanism) of the material [5,7,8,13,15–17].

Drying is thus useful to empty the porosity, as well as to stop ongoing hydration of hardened cement paste [18]. The difficulty of drying is to remove as much free water from the pore space as possible (otherwise known as pore water or capillary water) and, at the same time, as little interlayer water (also known as gel water) and as little chemically bound water as possible [18,19]. Desaturation, desorption, and dehydration phenomena associated with drying may generate damage like microcracking, capillary porosity evolution, collapse of fine pores, or mineralogical transformations [20]. The water should thus be removed without damaging the pore structure by capillary hydrostatic stresses due to receding water menisci [19], and without creating any modification of the porosity-mineralogical phases organization.

Drying can distort chemical and microstructural interpretations [21,22] so the pre-processing technique used must be considered [23]. Unfortunately, the ideal drying technique, which would preserve the microstructure and remove only the non-bound water, does not exist. All conventionally used drying techniques (e.g. oven, microwave, vacuum drying, D-drying, P-drying, freeze drying and solvent exchange methods) affect the microstructure in their own ways [20,22,24,25]. Removing water without changing the specimen's microstructure and chemical composition is extremely difficult or impossible to accomplish [23]; therefore, a choice has to be made according to the drying objectives [22,26,27]. Finally, all the direct drying methods remove only water without the ions dissolved in the pore solution, which can lead to artefacts, such as the formation of salts during drying [28].

Many studies have compared the effect of different drying methods on OPC-based cements [12,19,22,23,29,30], but very few have been carried out on alkali-activated binders (e.g. [12,17]). Zhang et al. [12] showed that the porosity of an AAM (based on metakaolin, fly ash and slag activated with sodium silicate solution) can be affected by drying at 65°C under vacuum, and by drying at 105°C in an oven. For these authors, low-calcium precursors (geopolymers) are less sensitive to the drying than the higher-calcium one (with GGBS). Their hypothesis is that the thermal stability of the geopolymeric gel is higher than that of C(-A)-S-H, but it can also be added that a smaller proportion of the mixing water is chemically bound in geopolymer than in GGBS-binder, and that the pore networks of these two types of materials differ considerably. Regarding the activator, based on a few precursors, Kovtun [17] showed that sodium metasilicate alkali-activated concrete appears to be more sensitive to drying than a sodium hydroxide-based one. However, due to the great variability of alkali-activated mixtures, as well as the singular behaviour of each of them, it seems delicate to make general remarks on the best method to use to dry all alkali-activated binders. It appears more appropriate to continue the investigations and give recommendations relating to precursor-activator couples.

The aim of this study is to evaluate the impact of drying on alkali-activated binders for temperatures ranging from 20°C to 125°C. The effect of drying time, primary vacuum and relative humidity content was also evaluated for some samples. For this study, four alkali-activated binders were compared with conventional binders based on OPC (CEM I) and OPC-GGBS (CEM III/B): a geopolymer (sodium-silicate activated metakaolin), a sodium-carbonate activated GGBS, a sodium-silicate activated GGBS, and a sodium-silicate activated mixture of 50 % metakaolin and 50 % GGBS. Pastes and mortar samples were first cured in autogenous conditions at 20°C for 28 days, and then dried in an oven until their mass stabilized.

First, the masses of the mortars were monitored during drying in order to assess the water loss of the materials. On these samples, non-destructive testing (NDT) was carried out before and at the end of

drying, as acoustic wave propagation velocity and electrical resistivity measurements. Then, destructive analyses (compressive strength and mercury intrusion porosimetry (MIP)) were performed on dried samples and on autogenous ones having the same age. Finally, to better understand a possible evolution of the phase assemblage generated by drying, X-ray diffraction, infrared spectroscopy and thermogravimetric analysis were performed on dried paste samples. All these data allow us to evaluate the effect of drying on the mechanical and microstructural properties of AAMs, and to discuss AAM drying recommendations for durability testing.

2. Material and methods

2.1. Raw materials

Six mixtures were prepared in this study, two conventional binders based on OPC (CEM I) and OPC-GGBS (CEM III/B) and four alkali-activated binders. The choice of the two OPC-based references was justified by the fact that AAMs are potentially intended for the same applications as OPC-based materials, and that there is much more data available on their drying (e.g. [12,19,22,23]).

The reference binders used in this study were, following European standard nomenclature (NF EN 197-1, 2012), a CEM I (CEM I 52.5 R CE CP2 NF) cement from Lafarge-Holcim (Le Teil, France) and a CEM III/B (42.5 N – LH/SR CE PM NF) cement from Lafarge-Holcim (La Malle, France), which contained 71% of GGBS. Chemical composition was measured by ICP-OES (Perkin Elmer) (Table 1; [31]).

For alkali-activated materials, metakaolin (Mk) precursor was manufactured by Argeco Développement (Fumel, France) by flash calcination of kaolinite, i.e. a few seconds at a temperature close to 700°C (see calcination details for this metakolin in San Nicolas et al. [32]). It contained mainly an amorphous metakaolinite phase and crystalline quartz, together with minor mineral phases such

as calcite, kaolinite, illite, mullite hematite and rutile (Table 2). The fact that there is more than 40 % of quartz in the metakaolin, of size less than 100 µm, makes the sample of geopolymer paste not really a paste but more like a 'mortar' with quartz fines. Chemically, metakaolin was composed of approximately two-thirds of SiO_2 and one-third of Al_2O_3, with a few percent of Fe_2O_3 (Table 1). Its density was 2.59 g/cm^3 and its specific surface area was 17 m²/g (BET analysis carried out at the CIRIMAT laboratory, using a Micromeritics Tristar 3020 apparatus with a degassing temperature of 350°C).

GGBS precursor was manufactured by Ecocem (Fos-sur-Mer, France). It was >95% amorphous slag with a basicity index CaO/SiO_2 of 1.2 (Table 1), a density of 2.93 g/cm^3, a Blaine specific surface area of 4633 cm^2/g and a 28-day activity index of 98% (NF EN 196-1, 2016).

Alkali-activated materials were prepared from a mixture of metakaolin and/or GGBS with sodium silicate solution or sodium carbonate powder. The sodium silicate was a commercial activation solution (Betol® 47T), from Woellner. It contained 55.5% by weight of water and 44.5 % of activator with an SiO_2/Na_2O ratio of 1.7, i.e. 27.5 % of SiO_2 and 16.9 % of Na_2O. Sodium carbonate was a >99% pure Na_2CO_3 powder with a density of 2.53 g/cm^3 from Solvay. Finally, tap water and standard quartz sand (0-2 mm) were used to prepare mortars according to the NF EN 196-1 (2016) mixing protocol.

2.2. Sample preparation

Four alkali-activated mortars with a water/binder (w/b) ratio of 0.4 were studied (see Table 3). W/b ratio was calculated from the sum of both the added water (tap) and the water of the activation solution, all divided by the sum of the activators' and precursors' dry masses. The first mixture was a metakaolin-based geopolymer developed by the LMDC laboratory. This mixture has been the subject of several publications, for example about formulation and performance [33,34] or robustness [35]. Two mixtures of activated GGBS were prepared, one with sodium carbonate activating solution and

157 one with sodium silicate (GGBS-carbonate and GGBS-silicate). Finally, a mixture of 50% metakaolin
158 with 50% GGBS activated by sodium silicate was assessed in this study (Mk-GGBS-silicate) to evaluate
159 the coupling of the two precursors. In order to better identify the crystalline phases in the mortars,
160 four paste mixtures were made, respecting the same raw material and water/binder ratios.
161 Practically, the mixtures were the same as those described for the mortars (Table 3) but without the
162 sand. OPC-based references were composed of mortars made from one CEM I cement and one CEM
163 III/B cement with a water/binder ratio of 0.5 (see Table 3) to obtain a similar consistency as assessed
164 by slump test with a small Abrams cone (height: 15 cm, diameters: 5 cm and 10 cm).
165
166 The mortar mixtures were made in a standardized mixer (Automix Control®) according to standard
167 protocol (i.e. 60 seconds at 140 ± 5 rpm with sand addition after 30 seconds, 30 seconds at 285 ± 10
168 rpm, 90 second pause, 60 seconds at 285 ± 10 rpm, NF EN 196-1, 2016). The activator was first
169 homogenized with water, then the precursor was introduced at the start of mixing, 30 seconds
170 before the addition of sand. Mortars were cast at 20°C into 4x4x16 cm^3 polystyrene moulds,
171 protected by films to prevent drying. The test pieces were cast in two steps followed by 10 seconds
172 of vibration on a vibrating table. Most of the samples were demoulded 24 hours after casting, with
173 the exception of the GGBS-carbonate mixture, which was demoulded at 48 hours because of its low
174 mechanical properties at early age. The specimens were then autogenously cured (wrapped in plastic
175 film and sealed in humidified plastic bags) for 28 days at 20°C. After this cure, some samples were
176 kept in autogenous conditions, others were dried at 20°C with several relative humidity values (0% in
177 vacuum dryer in air-conditioned room, 50% in air-conditioned room or 95% in wet room with
178 permanent showers), and the last samples were dried in an oven at 40°C, 50°C, 60°C, 80°C, 105°C or
179 125°C with no control of relative humidity. Note that the temperature in the wet room may have
180 varied between 14 and 25°C. Pastes were made with a KENWOOD kitchen mixer according to the
181 following protocol in five steps: liquid mixing for 2 min at slow speed, addition of powder, mixing for
182 1 min at slow speed and 1 min at fast speed, pause for 30 s, and mixing for 1 min at fast speed. The

pastes were cast into 4.5x7.5x2.5 cm^3 airtight plastic boxes for an autogenous cure of 28 days, then dried or kept in autogenous conditions.

2.3. Methods

2.3.1. Drying kinetics

The mortar bars were weighed at a precision of 0.01 g immediately after unmoulding (one or two days after casting), at the end of the 28-day autogenous cure, and several times a week during drying. When the mass had been stable for more than one week (mass loss less than 0.05 % in 7 consecutive days), the specimens were considered dry (large dots in Figure 1) and were then analysed using the methods described below. As drying at 125°C was faster than at 80°C, and drying at 80°C was faster than at 40°C, the test samples having undergone these treatments were not analysed at the same age (ages will be systematically specified). Due to the very long drying, it was decided to stop the drying step of samples stored at 20°C - 50 %RH after 7 weeks, and thus before mass stabilization. For the evaluation of drying kinetics, at least 4 samples were analysed for each condition and for each AAM material, but only two samples were analysed per condition for the reference OPC-based cement mortars.

2.3.2. Ultrasonic pulse velocity (UPV)

A non-destructive method was used to measure the ultrasonic pulse velocity (UPV), i.e. the propagation velocity of an electro-acoustic longitudinal wave (ultrasonic) in the mortars (EN 12504-4, 2005; ISO 1920-7, 2004). The machine used was a PUNDIT (Portable Ultrasonic Non-destructive Digital Indicating Tester), from Controlab Proceq, equipped with two P-wave transducers (54 kHz Ø

50 mm x 46 mm). Grease was used to make the contacts between the transducers and the 4x4x16 cm^3 mortar sample.

The ultrasonic pulse propagates through the gaseous, liquid and solid phases at 330 $m.s^{-1}$, 1480 $m.s^{-1}$ and from 2000 to 8000 $m.s^{-1}$, respectively (e.g. 5500 to 6000 $m.s^{-1}$ in quartz; [36,37]). In mortar, the UPV depends on several parameters ([38] and reference therein), such as the density and porosity of material [39–42], the degree of saturation of the porosity [43–46], the mechanical strength [41,47,48], microcrack formation [49,50], and temperature [51]. According to the mix design, the UPV of cementitious material lies globally in the 3000 and 5000 $m.s^{-1}$ range [46,52,53].

The UPV analyses carried out in this study were intended to follow the evolution of the mortars under autogenous conditions as well as to non-destructively characterize the evolution of mortar properties caused by drying. In order to limit the amount of data and associated figures, the UPV results are not displayed in the main text but are presented in Supplementary data BS2.

2.3.3. Electrical resistivity (r)

The resistivity / electrical conductivity of a mortar, which may be related to porosity and water content [54–56], was also measured by a non-destructive, method. According to availability, two machines were used: the first was an Ohmega resistivity meter, from Allied Associates Geophysical Ltd, working in resistance mode at I = 0.5 mA; the second was an assembly consisting of an AC generator operating at 1488 Hz, a voltmeter and an ammeter. The contact between the 4x4x16 cm^3 mortar specimen and the two electrodes fixed on metal grids was made with a wet sponge, the resistance of which (without sample) was also measured. Mortar bar resistivity (r) is given by Equation 1.

$$r = R \times S / L \qquad and \qquad R = U / I \quad (1)$$

with resistance $R = R_{mortar} - R_{sponge}$ (resistance of mortar and sponge, respectively); U: voltage in volts; I: intensity in amperes; S: contact surface area in square metres and L: length of the sample in metres.

2.3.4. Compressive strength (f_c)

A standardized 3R press was used for the mortar 4x4x16 cm^3 bar compression tests based on standard NF EN 196-1 (2016). Three tests in compression were performed for each sample instead of one test in bending and two tests in compression. All data are reported in Supplementary data A but only the average of these three results is shown in the figures of this article. Measurements were carried out on dry specimens and on control specimens stored under autogenous conditions for the same duration. In order to evaluate the dispersion of data, at least two specimens were analysed per drying condition for each mortar mixture (i.e. ≥ 6 measurements).

This destructive test method was coupled with non-destructive testing: acoustic wave propagation velocity and electrical resistivity (Supplementary data A; BS2). All these methods were carried out periodically on mixtures stored in autogenous conditions and on dried samples at the end of drying. The results are intended to complement the data on kinetics and efficiency of drying in order to specify the impact of drying on the materials concretely, and also to refine our hypotheses concerning the mechanisms involved.

2.3.5. Bulk density (ρ)

Autogenous and dried samples were placed in a desiccator under vacuum for 4 hours. Water was then injected into the desiccator to fully immerse the samples for 24 hours (with the vacuum maintained). Each soaked sample was then weighed under water (hydrostatic weighing M_{water}) and in

the air after being wiped (M_{air}). The samples were next dried for one week at 105°C to remove all water then weighed (M_{dry}). This protocol is described in more detail in the standard AFPC-AFREM (1997).

The apparent bulk density (ρ) was expressed in g·cm^{-3} following Equation 2, where ρ_{water} is the density of water, equal to 0.998 g·cm^{-3} at 20°C.

$$\rho = \frac{M_{dry}}{(M_{air} - M_{water})} * \rho_{water} \qquad (2)$$

2.3.6. Mercury injection porosimetry (MIP)

An AutoPore IV 9500 Porosimeter from Micromeritics was used up to a maximum mercury pressure of 400 MPa following the ISO 15901-1 (2005) standard. This allows information to be obtained on pore access diameters (throat-sizes) from 300 µm down to 3 nm, following Washburn's law with a mercury contact angle of 130° and a surface tension of 0.485 N.m^{-1} [57]. The samples were not dried again for the MIP analysis, in contrast to what is often recommended but is not mandatory [58]. Pieces of mortar of about 1 to 3 g per test were thus put directly into the penetrometer, and then dehydrated during the evacuation step in the porosimeter. Autogenous samples containing water were therefore dried during the evacuation step in the porosimeter, with a risk of this evacuation step inducing an additional modification of the pore network. The test did not start until the exhaust pressure was ≤ 50 µmHg (6.666 x 10^{-5} Bar) assuming complete evaporation of the free water. A test carried out on two geopolymer mortar samples removed from the penetrometer at the end of the vacuum, then placed at 105°C for 24 hours, confirmed that 80-90% of the mixing water had already been removed during vacuuming. Moreover, if a little free water, defined as that being linked to the rigid skeleton only by weak capillary forces, were to remain, the weakness of the capillary forces

should not hinder the passage of mercury [59]. For autogenous samples, the evacuation step could therefore last several hours. It was much quicker for previously dried samples.

It has been demonstrated that, if large pores are accessible by small throats, the mercury forced into the pore remains in it after the mercury pressure is decreased to atmospheric pressure [60]. This phenomenon, called trapping, was exploited by performing MIP analyses in two phases on our samples: intrusion and extrusion. MIP porosity ϕ and the pore size distribution, or more exactly pore access diameter distribution, were also evaluated. For that, in each analysis the intrusion volume was divided into several pressure groups, corresponding to pore size accesses of < 10 nm, 10-100 nm, 0.1-1 µm, 1-10 µm, 10-100 µm and > 100 µm as in [61]. Finally, the pore diameter that we noted d_{Hm1}, corresponding to half the volume intruded in the main intrusion peak (in nm) was evaluated. The objective of this indicator is to observe the evolution of the size of the finest pores (in the main intrusion peak), without being influenced by microcracking.

The notion of free and trapped porosities is not often used in civil engineering publications [62,63]. To summarize, the mercury intrusion allows the total connected porosity to be calculated. When the pressure returns to atmospheric pressure, part of the mercury remains trapped in the sample corresponds to the trapped porosity, it is represented by pore–throat arrangements with low throat-to-pore-size ratio. Analogously, voids with high throat-to-pore-size ratios, including cracks, are free of mercury at this stage since they do not entrap it [60]. By carrying out different cycles of intrusions and extrusions, Portsmouth and Gladden [64] and Mata et al. [65,66] saw that the volume of mercury looped on the same hysteresis cycle, which characterized the possibilities of privileged transfers within the porous system. The percentage of trapped mercury can be qualitatively correlated with the degree of porous network connectivity (α) (equation 3): the weaker α is, the more the material will be connected. Permeability is a complex notion determined by the ink-bottle effect, the size of the different pore families, and also the tortuosity and connectivity of the material.

Knowing the degree of connectivity of the pores (equal to the ratio of volume of mercury extruded to volume of intruded mercury) therefore makes it possible to understand some of the permeability properties of the material.

$$\alpha = \frac{\text{Volume of extruded mercury}}{\text{Volume of intruded mercury}} \qquad (3)$$

Due to the toxic and polluting characteristics of mercury and the complex management required for the contaminated samples after testing, only one analysis was conducted for each binder, drying and age. However, to verify the repeatability, several duplicates were analysed on some samples. In this case only the average and the confidence interval are displayed in the graphs.

2.3.7. Scanning Electron Microscopy (SEM)

Paste materials were observed with a JEOL JSM 3680 on polished surface. Cubic 1x1x1 cm^3 SEM samples were broken or cut from the paste samples with a circular saw. Samples were polished with ethanol using carbide polishing disks (Presi) (polishing discs and grain size: ESCIL, P800–22 µm, P1200–15 µm and P4000–5 µm). Then samples were coated with graphite and placed in the SEM chamber until a vacuum of 2.10^{-5} mBar was reached. Mineralogical phases and cracks were observed in backscattered electron detection mode.

2.3.8. X-Ray Diffraction (XRD)

Alkali-activated pastes were crushed manually in an agate mortar until a powder with particles < 40 µm (sieve control) was obtained. The diffractometer was a Bruker D8 Advance using a copper X-ray tube, equipped with a vertical theta / theta goniometer and a LynxEye XE-TTM high-speed linear detector. A motorized anti-scattering knife was used. The acquisition of the diffractograms was

carried out at 40 kV and 40 mA, from 7° to 70° 2θ with an interval of 0.02° 2θ and a total acquisition time of 2h30 per sample. Minerals were identified using the Bruker-AXS DIFFRACplus Eva v4 software and the 2015 ICDD PDF database. Metakaolin mineralogical quantification was performed by Rietveld calculation with DIFFRACplus Topas v5 following rules described in Trincal et al. [67].

2.3.9. Fourier-transform infrared spectroscopy (FTIR)

FTIR analyses were performed using a Perkin Elmer Frontier FTIR spectrometer. The analyses were made on a layer of crushed paste (< 80 µm) directly deposed on the diamond cell after measurement of the background in the air. The transmittance spectrum obtained was an accumulation of 12 measurements made between 4000 cm^{-1} and 600 cm^{-1}.

2.3.10. Thermogravimetric analysis (TGA)

The TGA method quantified the mass losses of a sample undergoing a temperature increase in a controlled atmosphere, in order to identify the chemical reactions or the phase changes that possibly occurred in the sample under heating [68,69]. Analyses were carried out using a Mettler Toledo TGA2 STAR^e system. For each sample, approximately 0.5 g of paste powders (< 80 µm) was heated in a 150 µL crucible, from 25 or 30°C to 1050°C with a ramp of 10°C/min under 50 mL/min of Argon.

3. Mortar characterization results

3.1. Water loss kinetics

Figure 1 shows the mass variations recorded during the different drying processes for the six mixtures, and Figure 2 reports the water content (V_w) of the mortars at the end of drying. For both

figures, dot and histogram colours are related to the temperature used for drying. It can be seen that, for both alkali-activated and OPC-based mixtures, the higher the temperature, the faster and more effective the drying process. These results follow exponential decrease laws and are consistent with the literature [23]. For instance, at 105°C and 125°C, 4x4x16 cm^3 mortar bars were considered fully dried after 2 or 3 days, while it was necessary to wait for about two or three weeks at 40°C to obtain mass stabilization, and almost two months at 20°C - 50 %RH (Figure 1). According to Kelvin's law at 20°C [70], the lower the relative humidity, the smaller the Kelvin radius (r_k) [71]. When the radius of a pore is higher than the r_k, it desaturates. In the case of the geopolymer [72], r_k = 51.97 nm for RH = 98%, 1.7 nm for RH = 54% and 0.95 nm for RH = 33%. The relative humidity was not controlled during oven drying. However, the geopolymer pore size was larger overall than in CEM- or slag-based mixtures, suggesting that, for a fixed humidity, the geopolymer will desaturate more quickly. It is therefore likely that temperature, relative humidity and pore size have a combined effect on drying kinetics.

Whatever the conditions, geopolymer and Mk-GGBS-silicate masses stabilized faster than those of the other four mixtures, suggesting higher water transfer properties. This is supported by the facts that the pore size varies according to the mixture, and that free water is more easily removed than chemically bound water. In geopolymer, there is mostly free water [3,73], while in CEM- or slag-based binders a large proportion of the water is physically absorbed and chemically bound in hydrates. To go further, the nature of hydrates is not the same in cement-based mortars as in those based on slag, and GGBS-OPC binders are known to have smaller pore size distributions than pure OPC. The chemical bonds between water and hydrates are therefore not the same, which can contribute to different drying kinetics. At the end of the autogenous cure, depending on the amount of air bubbles trapped during mixing, the degree of saturation of geopolymer porosity is close to 95-100% [72], while it is much lower in the other binders (water was emptied from the pores during

hydration). This is confirmed by the mass increase of cementitious and slag mortars when they are placed in the wet room, corresponding to a re-saturation of the porosity (Figure 2).

3.2. Strength properties

Figure 3 shows the compressive strength (f_c) of the four alkali-activated and the two CEM-based mixtures. In this figure, the dot colour is related to the temperature (as in previous figures); the vertical axis corresponds to the duration of drying (after 28 days under autogenous conditions) and the horizontal axis to mechanical strengths in MPa.

- Geopolymer stored in autogenous conditions had similar f_c values from 28 to 150 days (Figure 3A; Supplementary data A). Without water exchange, the geopolymer strength no longer evolved once the geopolymerization reactions were completed. Both ultrasonic pulse velocity (UPV) and resistivity results were also constant between 28 and 88 days (Supplementary data B), confirming that there was no material damage or evolution during this period. All these results are consistent with the literature, since most geopolymerization reactions take place in the first few days after casting [33,74].

After 28 days of autogenous cure, geopolymer dried at a temperature ≥ 50°C, and especially between 80°C and 125°C, induced a large f_c loss (of as much as 37 %; Figure 3A; Supplementary data A). This loss persisted with an extension of drying for several weeks (e.g. same f_c for samples dried for 14 or 60 days at 105°C). For drying at T ≤ 40°C, the dried geopolymer samples showed similar f_c to those stored in autogenous conditions. The UPV values of the geopolymer seemed to be modified in proportion to the intensity of drying. Samples cured in a wet room had identical results to autogenous samples of the same age. Samples dried at temperature T ≤ 40°C showed a very slight

412 decrease in UPV, and in those dried at T ≥ 60°C UPV dropped by about a quarter (Supplementary
413 data A; BS2).
414
415 Significant similarities observed between the UPV and f_c trends suggest a relationship between them,
416 and the possibility of evaluating geopolymer f_c with non-destructive UPV measurements. However,
417 this implies a calibration step to assess the contribution of each parameter: the porosity and its
418 degree of saturation, the microcrack occurrence, the mineralogical assemblage, etc. (see part 1.4.
419 Methods).
420
421 - GGBS-silicate and GGBS-carbonate conserved in autogenous conditions underwent a slow strength
422 increase from 28 to 88 days, and seemed stabilized beyond 6 months (Figures 3B and 3C;
423 Supplementary data A). Resistivity was 10 times higher than in the geopolymer and this value
424 increased over time (Supplementary data BS4). The resistivity of a material depends, among other
425 things, on its water content (open porosity and degree of saturation of the pores) and the
426 concentration of salts in the porous solution [56]. Resistivity increase in autogenous conditions can
427 thus be related to the continuation of hydration reactions over time through the consumption of
428 water or ions by the pores, also leading to strength increase. For these two mixtures, ultrasonic pulse
429 velocity values were stable over time, as for geopolymer but with higher values. The speed of
430 propagation of an electro-acoustic longitudinal wave depends on the properties of the medium it
431 crosses, which suggests that the two GGBS-based mixtures were denser and more rigid/less porous
432 than the geopolymer [38]. The geopolymer bulk density of 2.01 $g.cm^{-3}$ was indeed lower than those
433 of GGBS-silicate and GGBS-carbonate, with 2.16 $g.cm^{-3}$ and 2.11 $g.cm^{-3}$, respectively (Table 3).
434
435 For both mixtures, drying at T ≥ 80°C or at 20°C (whatever the humidity), did not decrease the f_cs,
436 which were similar to those of samples stored under autogenous conditions (Figures 3B and 3C).
437 However, drying at 60°C or, more significantly, at 40°C decreased the f_c by as much as 36 % and 24 %

438 for GGBS-silicate and GGBS-carbonate, respectively. This was not due to the time spent in the oven
439 since the samples kept in the oven for 2 months showed results similar to those analysed at the end
440 of regular drying. Further drying at 40°C - 80% RH was carried out on the GGBS-silicate. The results
441 were similar to those of autogenous samples, i.e. almost no water flow or strength modification,
442 suggesting that the temperature of 40°C affects the f_c only when humidity is low.
443
444 - Mk-GGBS-silicate stored in autogenous conditions showed a marked f_c increase between 28 and 88
445 days (Figure 3D; Supplementary data A). Ultrasonic pulse velocity results revealed an augmentation
446 over time in autogenous conditions while resistivity remained constant (Supplementary data A, BS2).
447 This suggests an increase in the density or rigidity of the material, without any drastic modification of
448 the pore solution. However, the bulk density remained constant at 2.08 $g.cm^{-3}$ (Supplementary data
449 BS1). These results suggest a combination of several reactions over time, such as hydration reactions
450 in the unreacted slag and recrystallization/restructuration of the geopolymeric gel.
451
452 Surprisingly, whatever the temperature used, the Mk-GGBS-silicate drying considerably reduced both
453 f_c (by between 30% and 45%) and UPV (by 25%) (Figure 3D; Supplementary data A, BS2). Only
454 samples cured in the wet room (20°C - 95% RH) presented results similar to those of autogenous
455 samples. Once dry, samples no longer showed f_c increases – unlike the autogenous one, in which the
456 f_c difference increased over time. This suggests that even the smallest loss of water caused by drying
457 at 20°C - 50 %RH, is enough to stop the chemical reactions, an observation that is probably related to
458 a humidity drop in the mortar. Other possibilities are development of cracking or even structure
459 degradation due to removal of water from the skeleton. This mixture thus seems very sensitive to the
460 evaporation of its water, more than geopolymer, despite very close water contents.
461
462 - The f_cs of CEM I and CEM III/B mortars were very stable over time between 28 and 88 days in
463 autogenous conditions (Figures 3E and 3F). Furthermore, neither of these two mixtures showed an f_c

drop due to drying. In contrast, CEM III/B showed an f_c increase of about a third for a drying temperature ≥ 80°C, which was probably related to an acceleration of hydration reactions by the thermal curing [75,76]. On CEM III/B concrete samples, Azar et al. [77] observed an f_c increase of 15 % with drying at 40°C.

3.3. Porosity

Mercury intrusion porosimetry (MIP) data are reported in Table 4 and illustrated Figure 4. For each AAM, Table 4 gives three parameters: the connected total porosity (ϕ) in %, the degree of pore connectivity (α) in %, and the pore diameter (d_{Hm1}) in nm corresponding to half of the mercury volume intruded in the main intrusion peak. According to the pore size distribution (supplementary data BS5), the main intrusion peak was bounded between 3 and 1000 nm for geopolymer, and between 3 and 225 nm for all other AAMs. All the larger pores (i.e. > 1000 nm or > 225 nm, respectively) appear to have been formed by microcracking due to preconditioning and were not integrated in the d_{Hm1} parameter. All ϕ, α and d_{Hm1} data are given according to drying and time (0 corresponds to the end of the cure, i.e. after 28 days in autogenous conditions, when samples were placed in drying or maintained in autogenous conditions). The reason why there is no confidence interval given in Table 4 is that only one sample was analysed, as good repeatability had been shown for other samples.

Figure 4 shows the evolution of the pore access diameter distribution, called pore size distribution, of the four AAM mixtures dried or stored in autogenous conditions. For each mortar analysed, intrusion volume was divided into six pore size groups: < 10 nm, 10-100 nm, 0.1-1 µm, 1-10 µm, 10-100 µm and > 100 µm. To achieve this, the intrusion volume was calculated between the pressure stages corresponding to the sizes of intruded pores as performed in Ortega et al. [61]. We recall that, if it is necessary for the mercury to pass through smaller capillaries to fill large pores (ink bottle effect),

490 then the measurement made by MIP will give a pore access diameter equal to the size of the smallest
491 capillaries [78].
492
493 Geopolymer mortar stored in autogenous conditions has an MIP porosity close to 18 %, which might
494 decrease slightly over time but, due to the accuracy of the measurements, more analyses would be
495 necessary to confirm this trend (Table 4). The pore access sizes distribution is monomodal, centred
496 around 7 nm (Table 4; Supplementary data BS5). Most of the mercury is introduced into samples for
497 pore access sizes between 5 and 20 nm, which corresponds to two categories in Figure 4 (< 10 nm
498 and 10-100 nm). In autogenous conditions, the geopolymer pore size distribution seems to remain
499 stable over time, as confirmed by d_{Hm1} (Table 4). Between 3 and 1000 nm (main intrusion peak), half
500 of the intruded mercury volume corresponds to a pore size d_{Hm1} = 9 nm, whatever the autogenous
501 cure duration. These results are consistent with literature data, according to which the pore volume
502 is stable over time and there are two pore families: first, a mean pore size generally close to 5-10 nm
503 depending on the water content, and second a porosity visible at microscale by microscopy but
504 invisible in MIP due to the ink-bottle effect [34,79]. Finally, for these autogenous samples, there is as
505 much free as trapped porosity; the connectivity of the porous network is high (α close to 50%; Table
506 4).
507
508 The more intense the drying, the greater the MIP porosity (up to 23.5 % for drying at 105°C), and the
509 greater the size of the pore accesses (Table 4; Figure 4B). Whatever the conditioning, with the
510 exception of the humid room (at 20°C-95 %RH), which is not a desiccant condition, drying induces an
511 increase in the d_{Hm1} which can be associated to drying shrinkage and formation of microcracks (Table
512 4; Supplementary data BS5). The d_{Hm1} doubles with drying at 20°C, quadruples at 40°C, and is
513 multiplied by ten for a temperature ≥ 80°C. This results in a change of the pore size categories in
514 Figure 4B, where, above 40°C, there are no more pores < 10 nm and, above 80°C, the 0.1-1 µm pore
515 category becomes the most abundant. These variations could be the consequence of material micro-

516 cracking and/or the collapse of the walls between the smaller pores. This seems to be confirmed by a
517 slight decrease in α to 44.5 at 125°C (Table 4), suggesting a higher connectivity of the porous
518 network.
519
520 GGBS-silicate and GGBS-carbonate mortars stored in autogenous conditions for more than 28 days
521 were less porous than geopolymer, with total accessible porosities around 12% and 15% respectively
522 (Table 4; Figures 4C; 4E). However, the reproducibility of the analyses was not very good (in
523 particular for GGBS-carbonate with porosity differences of up to 4% between two samples) and the
524 intrusion curves show that these samples were not saturated with mercury. This last point indicates
525 that, unlike in the geopolymer, there were pores smaller than 3 nm. With a different liquid surface
526 tension, the water porosity measurements confirmed MIP data, with GGBS-based mortars having a
527 porosity close to 17 %, compared with 21 % for the geopolymer (Supplementary data BS5). The pore
528 size distribution was monomodal < 30 nm for the GGBS-silicate, with an average d_{Hm1} of 6.5 nm and α
529 close to 67 % (Table 4; Figures 4C). For GGBS-carbonate, the pore size distribution was monomodal <
530 50 nm with an average d_{Hm1} of 9.2 nm and α close to 60 % (Table 4; Figures 4E). Note that, for this
531 last binder, both d_{Hm1} and α seem to have decreased during the autogenous cure. The connectivity of
532 the porous network in GGBS-binder is thus lower than in geopolymer, the pore size is different, as is
533 probably the case for the ink-bottle effect and the tortuosity, so the permeability is very likely to be
534 different between the metakaolin and slag-based binders. This can have repercussions on water
535 transfers and drying kinetics (Figure 1).
536
537 With drying, no mixtures stored at 20°C (at relative humidity of 0 %, 50 % or 95 %) appear to have
538 been significantly affected. The ϕ, α and d_{Hm1} have similar values (Table 4), and the pore size
539 distribution also appears to be identical (Figures 4D; 4F). In contrast, GGBS-binders dried at 40°C or
540 more show a significant increase of the d_{Hm1}, to the extent of being quadrupled. This results in a drop
541 of the pore access category < 10 nm in favour of the 10-100 nm and > 1 µm ones (Figures 4D; 4F).

Regarding the MIP porosity, for GGBS-silicate, ϕ is higher for samples dried at 40°C than for those stored under autogenous conditions, but lower than those dried at T ≥ 60°C (Table 4). For GGBS-silicate, ϕ is higher for samples dried at T ≥ 60°C than for all the others. The connectivity of the pores appears to be maximum for the GGBS-silicate dried at 40°C; while it appears minimum for GGBS-carbonate dried at T ≥ 60°C. For these two AAMs, drying at 40°C seems to have different effects from drying at T > 60°C, suggesting micro-cracking formation (as for geopolymer) or assemblage phase transformation.

Mk-GGBS-silicate mortar stored in autogenous conditions showed a MIP porosity content lying between those of the geopolymer and the GGBS-silicate and decreasing over time (Table 4). The d_{Hm1} was close to 6.8 nm, smaller than the geopolymer value, and the pore access diameter distribution was below 20 nm. According to the intrusion curves, these samples were not saturated with mercury, suggesting a pore size population below 3 nm. By grouping the pore access diameters by classes, half the Mk-GGBS-silicate samples were found to have porosities of < 10 nm at the end of the cure, while this value reached three quarters 6 months later (Figure 4G). Like ϕ, the connectivity of the porous network of GGBS-binder seems to be between those of the geopolymer and the GGBS-silicate.

With drying, all tested conditions resulted in ϕ, d_{Hm1} and pore connectivity increases (α decrease) (Table 4). This led the pore access diameters category < 10 nm to be replaced by the 10-100 nm one (Figure 4H). This material thus behaves similarly to the geopolymer, despite the fact that the use of slag has reduced its porosity.

4. Paste characterization results

According to previous results on mortar, AAM pastes may also be affected by drying. Note that for geopolymer and Mk-GGBS-Silicate pastes, the use of a pure metakaolin as raw materials (the used

568 one contains more than 40% of quartz, Table 2) could induce different behaviors. Depending on the
569 mixtures and the temperatures used, several phenomena can come into play: microcracking, phase
570 dehydration, degradation or recrystallization, etc. In order to clarify these hypotheses, paste samples
571 were cast, stored in autogenous conditions then dried before microscopic observations and
572 mineralogical identifications.
573
574 **4.1. Scanning Electron Microscopy (SEM) observations**
575
576 Geopolymer paste stored in autogenous conditions or dried at 40°C showed a network of reticulated
577 cracks, i.e. with primary large cracks (5-10 µm wide) that could be followed over several mm, as well
578 as secondary and tertiary finer cracks (Figure 5A; Supplementary data BS6). These cracks were
579 probably produced by the SEM vacuum [80] and/or by drying shrinkage.
580 Most cracks occurred preferentially at the interface between the geopolymer and quartz grains
581 which were initially present in the metakaolin. On the other hand, only a few cracks appeared
582 between the remaining undissolved metakaolin grains and the geopolymer paste. The geopolymer
583 paste seemed generally unaltered by drying at $T \leq 40°C$.
584
585 With drying at 60°C (Supplementary data BS6) or 105°C (Figure 5B), the geopolymer microstructure
586 was different. Fewer large cracks were visible, most likely because most of the drying shrinkage had
587 already taken place before SEM sample preparation, during the oven step. The cracks were narrower
588 than in autogenous samples and did not have a reticulated network. The geopolymer paste seemed
589 less dense and less homogeneous (looking more cavernous, corroded, with grain detachment),
590 suggesting that drying at 60°C or more induced a textural modification of the geopolymeric gel,
591 possibly micro-cracking, and an increase of visible porosity.
592

GGBS-silicate and GGBS-carbonate pastes seemed to have the same behaviour. In autogenous conditions, as the paste dried for 60 days at 20°C-65% RH, they showed a mosaic of small cracks (Figures 5C) that seemed to form preferentially at the slag/grain interface and were probably caused by desiccation induced by slag hydration (autogenous shrinkage) or desiccation in the vacuum chamber of the microscope [81]. Supplementary, bigger cracks were observed for GGBS-carbonate compared to GGBS-silicate, possibly explained by a greater autogenous shrinkage coupled with the slightly lower strength of the material.

With drying at 40°C, 60°C or 105°C, desiccation shrinkage induced large cracks (Figures 5D; 5E; 5F; Supplementary data BS6). A network of secondary cracks was also observable for samples dried at 40°C and 60°C (Figures 5D; 5E) but not for the one dried at 105°C (Figure 5F). Drying at 105°C therefore appears to be less damageable than drying at 40-60°C, suggesting that drying intensity and speed have an effect on the GGBS-binder microstructure. Similarly to geopolymer, the paste seemed less dense and less homogeneous after drying.

Mk-GGBS-silicate paste cured in autogenous conditions presented a network of cracks intermediate between that of the geopolymer and that of GGBS-silicate (Figures 5G; Supplementary data BS6). The micro-cracks crossed the matrix and ran along the grains of quartz and slag, which seems to indicate good grain-matrix cohesion.

Whatever the drying temperature (40°C, 60°C or 105°C), the texture of the paste seemed to be affected (Figure 5H) and looked like geopolymer dried above 40°C or the GGBS-silicate at 40°C or 60°C. The behaviour of Mk-GGBS-silicate therefore seems to be intermediate between those of the geopolymer and the GGBS-silicate.

4.2. Mineralogical analyses

618 X-ray diffractograms of geopolymer kept in autogenous conditions showed a mainly amorphous
619 material with crystallized phases, mainly quartz (SiO_2), and minor phases such calcite ($CaCO_3$),
620 hematite (Fe_2O_3), mullite ($3Al_2O_3.2SiO_2$), anatase and rutile (TiO_2) and other phyllosilicates (kaolinite
621 ($Al_2Si_2O_5(OH)_4$) and illite/muscovite probably ($K(Al,Mg,Fe)_2(Si,Al)_4O_{10}[(OH)_2,(H_2O)]$) (Figure 6A). The
622 FTIR spectrum (Figure 7A) exhibited the asymmetric stretching vibration of Si-O-T bonds (where T is
623 tetrahedral silicon or aluminium related to geopolymeric gel) close to 985 cm^{-1} [82,83], and Si-O out-
624 of-plane bending vibration at 693 cm^{-1} [84]. It also confirmed the presence of carbonate since
625 vibration of O-C-O bonds between 1430 and 1390 cm^{-1} was observed [85]. The TGA spectrum (Figure
626 8A) pointed out three weight losses: a first, main one generally attributed to the loss of water within
627 the porosity of the materials from 80°C to 250°C, a small second one between 300°C and 600°C
628 attributed to the release of water by condensation/polymerization of Si–OH and Al–OH groups, and a
629 third one between 600°C and 800°C related to the decomposition of carbonate species [86].
630
631 Whatever the drying temperature, no mineralogical changes were observed on X-ray diffractograms
632 for geopolymers kept at 40°C, 60°C, and 105°C (Figure 6A). However, the hotter the drying was, the
633 less marked was the amorphous hump. This may have been due to porous solution crystallization
634 during drying or a change in the structure of the amorphous gel as suggested by SEM observations
635 (Figures 5A; 5B). TGA analyses and FTIR spectrum (H-OH peak close to 1646 cm^{-1}) exhibited a
636 decrease of water within the materials, which became greater with temperature (Figures 7A; 8A).
637 Water loss with drying up to 105°C did not seem to change the mineralogy of the geopolymer, as
638 mainly free water in the porosity seemed to be removed. In the TGA spectrum, the decrease in the
639 signal of free water (80-120°C) in the porosity revealed the presence of a second signal attributed to
640 physically bound water (150-200°C). It might be water bound in the hydration shell of the sodium
641 counter ions [87,88].
642

GGBS-silicate autogenous paste diffractograms showed broad peaks (at 20-38° and 49-51°) assigned to amorphous phases and C-S-H / C-A-S-H (PDF file 33-0306; Figure 6B). These identifications were confirmed by Si-O-T bond peaks in FTIR spectra (Figure 7B), and also by weight loss between 105°C (loosely bound water) and 500°C (tightly bound water) on TGA spectra, corresponding to the evaporation of free water and interlayer water, and then the dehydroxylation of C-S-H / C-A-S-H close to 700°C (Figure 8B, [89–91]). Tobermorite ($(CaO)_x$-SiO_2-zH_2O, PDF file 06-0010) and hydrotalcite ($Mg_6,Al_2CO_3(OH)_{16}$-$4H_2O$, PDF file 14-0191) (Figure 6B) were observed in our autogenous samples, as cited in the literature [12]. On X-ray diffractograms, we observed that carbonation creating calcite and vaterite ($CaCO_3$) easily occurred when GGBS-silicate pastes came into contact with air.

After drying at 40°C for 35 days, 60°C for 24 days or 105°C for 14 days, GGBS-silicate pastes did not show mineralogical changes on X-ray diffractograms. Only a very slight decrease of the main amorphous hump was observed in X-ray diffractogram for 105°C drying (Figure 6B), probably due to dehydration of some C-S-H / C-A-S-H [90,91]. FTIR spectra and TGA thermograms also confirmed that there was no mineralogical modification due to drying, except for a different water loss (Figures 7B and 8B). With drying, less loosely bound water was noticed (up to 200°C) and a little more bound water (up to 500°C), that might be explained by the ongoing hydration of GGBS-silicate pastes over time, and potentially more C-S-H / C-A-S-H phases formed.

GGBS-carbonate pastes kept in autogenous conditions showed, as for GGBS-silicate samples, the presence of an amorphous hump on X-ray diffractograms, probably related to C-S-H / C-A-S-H phase (Figure 6C). Calcite, gaylussite ($Na_2Ca(CO_3)_2{\cdot}5H_2O$, PDF file 21-0343) and hydrotalcite ($(Mg_{0.667},Al_{0.333})(OH)_2(CO_3)_{0.167}(H_2O)_{0.5}$, PDF file 89-0460) were also detected. In FTIR spectra, the 1350-1550 cm^{-1} band and the shoulder at 871 cm^{-1} refer to the carbonation products in the paste (Figure 7C; [92]).

X-ray diffractograms on GGBS-carbonate revealed mineralogical variations after drying, (Figure 6C). With drying at 40°C, gaylussite peaks decreased in intensity and calcite peaks increased, while at 60°C and 105°C, there was no more gaylussite and the calcite appeared even more abundant (Figure 6C). The increase in calcite, however, was not confirmed by TGA, where the mass loss at around 700°C remained similar (Figure 8C). Calcite and hydrotalcite were present in all samples and seemed not to be affected by drying. An evolution of the carbonate compound structures of GGBS-carbonate paste thus seemed to be observed by X-ray diffraction. Like GGBS-silicate, GGBS-carbonate drying led to less loosely bound water being found in TGA analyses, and a little more bound water (Figure 8C). FTIR spectra also attested to the carbonate evolution, where O-C-O bound peaks had very different shapes depending on the drying, especially for drying at temperatures up to 60°C (Figure 7C).

Mk-GGBS-silicate pastes were a combination of minerals found in geopolymer and in GGBS-silicate pastes. On the X-ray diffractogram, autogenous samples showed an amorphous hump (probably combining geopolymer matrix and C-S-H / C-A-S-H phases), quartz, calcite, hematite, mullite, anatase and other phyllosilicates (kaolinite, illite/muscovite) (Figure 6D). The FTIR spectrum was consistent with the suggested mix of geopolymer matrix and GGBS-silicate matrix, since Si-O-T bands (960 – 967 cm^{-1}) were observed between 985 cm^{-1} (geopolymer) and 950 cm^{-1} (GGBS-silicate) (Figure 7D). The TGA spectrum was similar to the geopolymer one but with slightly more water loss between 200°C and 500°C confirming the presence of C-S-H / C-A-S-H phases (Figure 8D).

Few mineralogical changes were visible after drying. There was a slight decrease in the amorphous hump on XRD diffractograms at 40°C, 60°C or, more significantly, at 105°C, suggesting an evolution of geopolymer matrix and C-S-H / C-A-S-H phases (Figure 6D). Then, FTIR spectra showed slight variations in the O-C-O bond related to carbonates (Figure 7D), which were confirmed by slight variations in the TGA weight loss around 660-680°C (Figure 8D).

5. Discussion

5.1. Summary of behaviour of alkali-activated materials under drying

Most of the data in this article are summarized in Figure 9. They showed that CEM I and CEM III/B mortars were not mechanically damaged whatever the drying temperature (20°C to 105°C). The compressive strengths at each maturity time were equal to the ones of the reference sample kept in autogenous conditions (Figure 3E), and even increased for CEM III/B after drying at 80°C and 105°C (Figure 3F). This was probably related to an acceleration of hydration of slag by thermal curing [75,76]. However, different behaviours were observed for alkali-activated materials (Figure 9).

For the four alkali-activated materials, the higher the drying temperature was, the faster and the more effective was the drying (Figures 1, 2). Drying the geopolymer and MK-GGBS-silicate at 20°C, 40°C and 105°C, removed respectively 50 %, 65 to 68 %, and 80 % of mixing water, while drying the GGBS-silicate and GGBS-carbonate at the same temperature removed 10 to 20 %, 48 to 58 % and 72 % of mixing water, respectively (Figure 9A). This lower evaporation rate for slag and cement-based systems can be explained by the smaller pores, which remain saturated and the presence of hydrated phases. In addition, damage in AAMs could be observed to depend on the drying (Figures 9B and 9C):

- Geopolymer dried at a temperature ≥ 50°C, and especially between 80°C and 125°C, induced a significant compressive strength loss (of up to 37 %). This correlated well with a drop of about a quarter in the ultrasonic pulse velocity, which is a technique commonly used to follow the damage evolution in materials [41,47,48].
- GGBS-silicate and GGBS-carbonate strengths were not affected by drying at T ≥ 80°C or at 20°C (whatever the humidity). However, an f_c loss was observed with drying at intermediate temperatures: 40°C and 60°C with low relative humidity. In the meantime, all samples dried

721 at T ≥ 40°C had a large UPV decrease. It is therefore not currently conceivable to assess the
722 strength of GGBS-silicate (unlike geopolymer) materials with this NDT method, but rather to
723 detect the formation of microcracks.
724 - MK-GGBS-silicate was damaged whatever the drying temperature (30% to 45% strength
725 loss), combining the weak points of both geopolymer and GGBS-silicate materials.
726
727
728 **5.2. Mechanisms**
729
730 **5.2.1. Geopolymer**
731
732 No mineralogical changes able to explain the compressive strength losses were detected by visual
733 observation of XRD (Figure 6A), FTIR (Figure 7A), or TGA (Figure 8A), although a decrease in water
734 content was demonstrated with all these methods. A detailed statistical analysis of these spectra
735 could, however, refute this overall interpretation. As it dries, the pore solution should precipitate
736 phases that were not detected in XRD, possibly because they occurred in too small a quantity, or had
737 a composition similar to the gel. SEM observations also showed microstructural modification (Figure
738 5), with a less dense geopolymer paste and the apparition of porous zones. The decrease in strength
739 and the modification of microstructure is consistent with Llyod's work [93] comparing metakaolin-
740 based geopolymer before and after a heat treatment at 95°C. However, contrary to this study, no
741 zeolite was formed in our case after the heat treatment – or the amount formed was too low to be
742 detected by XRD even at 105°C or 125°C. The abundance of quartz in metakaolin could also have an
743 influence on the modification of the microstructure, which could possibly be avoided by using a purer
744 metakaolin as raw material.
745 Nevertheless, SEM observations (Figure 5) showed that drying at 40°C or less induced no visible
746 textural modification of the geopolymeric gel. These observations could be explained by a drying

747 shrinkage which increases as more free water is removed from 20 to 125°C [73,94]. Kuenzel et al.
748 [94] attributed this shrinkage event to capillary strains in the sample following the loss of free water
749 and concluded that the hydration spheres of Na^+ cations play a significant role in maintaining the
750 structural stability of the paste.
751
752 **5.2.2. GGBS-silicate and GGBS-carbonate**
753
754 For both slag-based AAMs, drying at T ≥ 80°C induced an increase in the pore size (Figure 9E), but did
755 not cause mineralogical change (Figures 6; 7; 8), additional cracking (Figure 5) or significant
756 mechanical strength damage (Figure 9B). Conversely, drying at 40°C and 60°C (with low RH) induced
757 significant compressive strength losses (Figure 3). This time, strength loss can probably be attributed
758 to carbonates and C-(A)-S-H reactions, possibly due to intercrystallite pores desaturation, dissolution-
759 precipitation, recrystallization or carbonation which may affect the porosity of the binder. This is
760 supported by changes in the structure of the hydrated products observed in GGBS-silicate dried at
761 60°C by Ismail et al. [10]. However, the results of our study do not allow us to conclude on a
762 mineralogical change due to drying (Figures 6; 7; 8). The kinetics of these reactions should be studied
763 in detail with the support of thermodynamic data. Since GGBS-silicate MIP porosity seemed to
764 increase for drying at 40°C (Table 4; Figure 4B) and SEM observations showed that the texture of the
765 gel was affected and looked like geopolymer paste dried at 60°C or 105°C (Figure 5), shrinkage and
766 micro/nano-cracking might occur, reducing mechanical strengths and creating voids.
767
768 Many authors have shown that, for a fixed temperature, relative humidity has a strong effect on the
769 material during drying [95]. Ye et al. [96] and Jia et al. [97] showed that the lower the relative
770 humidity and drying rate, the higher the shrinkage for alkali-activated slag materials, and so the
771 higher the chance of crack appearance. Drying at 40°C with a relative humidity of 80 % did not impact
772 the compressive strength of GGBS-silicate (Figure 3B). In Europe, a relative humidity of 50-65 % is

773 very common, but the temperature rarely stays at 40°C for long. In contrast, in arid deserts (e.g.
774 Sahara, Atacama, Namib), it is common to have 40°C with a very low RH. Inversely, in a humid
775 tropical environment it is common to have 40°C with a humidity close to 100 %. Depending on the
776 country, the temperature/relative humidity pair will vary and therefore play an important role during
777 drying, which can potentially affect the mortars differently.
778 Using Kelvin's law, it is possible to calculate the Kelvin radius (r_k) for mortar exposed at 40°C and both
779 20 and 80 %RH. According to Kelvin's law, with 40°C-20 %RH, the pores that are desaturated are
780 larger than 0.4 nm while, with 40°C-80 %RH it is only pores larger than 2.8 nm that are desaturated,
781 limiting the drying shrinkage. With a humidity rate of 80%, C-(A)-S-H intracrystallite pores were
782 desaturated ($0.6 \leq r \leq 1.6$ nm) while, with a humidity rate of 20% there were also intercrystallite
783 pores ($r \leq 0.6$ nm) [98,99]. It would therefore seem that the loss of mechanical resistance of a binder
784 is linked to the emptying of the intercrystallite C-(A)-S-H pores, inducing coarsening of pore structure,
785 probably attributable to the polymerization of silicate anion chains and the development of a
786 cohesive structure [100]. Some AAM are sensitive to moisture and may undergo a continuous
787 sequence of irreversible decomposition reactions during drying [11]. GGBS-silicate stored at 40°C
788 under autogenous conditions, or dried at 40°C – 80% RH, desaturated C-(A)-S-H intracrystallite pores
789 but not intercrystallite ones, which do not lead to a mechanical strength drop (Figure 3,
790 Supplementary data A). Nevertheless, this invites further investigation of the role of humidity and its
791 coupling with temperature.
792
793 One hypothesis to explain why the effect of desaturation at temperatures higher than 60°C did not
794 affect the compressive strength is that the kinetics of the drying is also of importance. At 60°C or
795 more, the material may be subjected to a shorter period of mechanical stress, limiting
796 microstructural damage. Ye et al. [96] and Hojati et al. [101] reported that their fine pore structure
797 and high degree of saturation found upon drying increased the effective capillary pressure, and slag
798 mixtures also showed a significant time dependent response (creep), where the pastes continued to

799 shrink after their maximum mass loss had been reached. Investigations by Ye and Radlińska [102]
800 and Ye et al. [103] have explained the high drying shrinkage of AAS by providing an understanding of
801 the behaviour of hydration products during the drying process. According to their research, the
802 structural incorporation of alkali cations in C-A-S-H reduces the stacking regularity of C-A-S-H layers
803 and facilitates their collapse and redistribution upon drying. The high drying shrinkage of AAS can be
804 attributed to the relatively low creep modulus of the hydration products in AAS.
805
806 **5.2.3. Mk-GGBS-silicate**
807
808 Intense micro-cracking was observed for mortar stored under autogenous conditions (Figure 5), and
809 was probably linked to a significant autogenous shrinkage favoured by the hydration of the slag.
810 Whatever the drying condition is, an increase in the pore size was observed (Figure 4), which could
811 be associated with nano-cracking and creation of porosity caused by drying shrinkage. As for the
812 geopolymer, the microstructure evolution could also be linked to the presence of quartz in the
813 metakaolin. As observed in another ternary mixture, a GGBS/fly ash geopolymer, the loss of water
814 related to drying is possibly related to the gel moving toward a less ordered and more cross-linked
815 structure [10]. Thus, both autogenous and drying shrinkage would probably be at the origin of the
816 drop in mechanical strength (Figure 9B), without there being any apparent mineralogical variation
817 (Figure 6).
818
819 Whatever the nature of the AAM, increasing the drying temperature (20°C to 125°C) induced no
820 mineralogical change but did lead to microstructural modifications due to autogenous and drying
821 shrinkage: disappearance of the smallest pores (< 10 nm) in favour of larger ones (10-100 nm, and
822 even 0.1-1 µm for geopolymer) that can be observed in SEM pictures and suggests the collapse of
823 fine pores with reorganization of the paste, and micro-cracking.
824

825 **5.3. AAM drying recommendations**

826

827 Experimental results in this manuscript refer to only four mixtures, without evaluation of their
828 robustness or the variability of raw materials. Starting with a different precursor or activator, in
829 terms of fineness, mineralogical or chemical composition, degree of crystallinity, etc., might lead to
830 significant differences in the experimental results. For example, the density and purity of metakaolin
831 governs its reactivity, as well as its autogenous deformation, which can be shrinkage or expansion
832 [104]. Likewise, the chemical composition of slag will determine its reactivity [105,106]. As shown in
833 numerous studies, activator dosage, water content and molar ratios will also influence the properties
834 of the alkali-activated material [94]. So, it should be kept in mind that the recommendations listed
835 below are valid for the raw materials and mixtures that we have tested, and should only be
836 generalized with caution.

837

838 Geopolymer (metakaolin rich in quartz activated with sodium silicate) showed a drop in mechanical
839 strength with oven drying at temperatures of 50°C to 125°C (Figure 3). This damage was correlated
840 with an increase in both MIP porosity and pore size (Table 4; Figure 4A) but, counterintuitively, fewer
841 large cracks were observed under SEM (Figure 5). It is likely that drying at over 50°C induced nano- to
842 micro-cracking, which damped the stresses generated by drying shrinkage and/or when the sample
843 was vacuumed in the SEM chamber, and thus prevented the formation of large fissures.
844 Oven drying at 40°C or less reduced the efficiency of drying, but retained mechanical properties (at
845 least 90% of strength of autogenous samples, Figure 9B). It did not seem to generate supplementary
846 micro-cracks, even though the pore size distribution began to be affected (Figures 4; 9D; 9E). No
847 mineralogical variation of the crystallized phases was observed between autogenous samples and
848 those dried at 40°C or 105°C (Figures 6; 7; 8). Oven drying at a temperature of 40°C appears to
849 provide a good compromise between quite efficient drying and little resulting damage, even if not all
850 free water is removed. This implies that standard methods requiring drying at 100-110°C should be

851 used with caution with metakaolin geopolymer (e.g. ASTM 642, 2006; Australian Standard AS1012,
852 1999; [107]). Finally, it seems that the only method found to preserve very small pores is freeze-
853 drying (Zhang et al. [12]; Supplementary data BS7). These findings are consistent with a study on OPC
854 by Konecny and Naqvi [108]. However, the method is not technically feasible with big samples, such
855 as on samples of 4x4x16 cm^3or bigger concrete samples.
856
857 GGBS-silicate and GGBS-carbonate mixtures have very different mineralogical compositions (Figure
858 7) but show globally similar behaviour during oven drying. For temperatures from 80°C to 125°C,
859 drying is fast and efficient (Figures 1; 2), strength properties do not appear to be affected (Figure 3)
860 and it seems that there are no new micro-cracks (Figure 5). In contrast, for both mixtures, oven
861 drying at 40°C to 60°C (at low relative humidity) induces a large compressive strength loss (Figure 3),
862 affects porosity (Table 4, Figures 4, 9), and generates micro-cracks (Figure 5). Compressive strength
863 loss was also observed on GGBS-carbonate concretes oven dried at 40°C [77]. Considering the
864 results, GGBS-based binder preconditioning should not include drying at 40-60°C but use a
865 temperature of at least 80°C to ensure quick drying. This is contrary to what is recommended in
866 some standard methods (e.g. ASTM C1585, 2011; EN 13057, 2002) or AAM studies [11]. As a
867 precautionary measure, it would be advisable to systematically assess the influence of
868 preconditioning by mechanical strength measurement before continuing with the durability tests.
869
870 Mk-GGBS-silicate was designed to combine the advantages of geopolymer and GGBS-silicate
871 systems. This seems to have been the case in view of the properties of the samples stored under
872 autogenous conditions. Unfortunately, during drying, Mk-GGBS-silicate mixture rather seems to
873 accumulate the disadvantages of both. Whatever the temperature used in the 20°C to 125°C range, a
874 significant drop in mechanical strength is observed after drying (Figure 3). This damage is correlated
875 with porosity and pore size increase (Table 4; Figures 4; 9), micro-crack formations (Figure 5) and
876 mineralogical variations (Figures 6; 7; 8). For this mixture, it is not possible to recommend a drying

877 temperature and other solutions may need to be considered, such as freeze drying, solvent
878 replacement drying [10,12,109] or supercritical drying [110,111]. However, these methods are more
879 costly and less practical. Vacuum drying is an often-used technique, tested here on geopolymer and
880 GGBS-silicate, but appears to be quite inefficient (Figure 1). Although the 50-50 metakaolin-slag
881 mixture results in an uninviting finding, requiring special precautions for durability tests, other
882 mixtures with one precursor more abundant than the other have shown much more encouraging
883 behaviour (not presented in this study) and deserve to be studied further.

884

885 **6. Conclusions**

886

887 Effects of drying with several temperatures from 20 to 125°C have been evaluated on four alkali-
888 activated mixture binders: a geopolymer (sodium silicate activated metakaolin), a sodium carbonate
889 activated GGBS, a sodium silicate activated GGBS and a sodium silicate activated mixture of 50 %
890 metakaolin with 50 % GGBS. Mixture robustness and variability of the raw materials were not
891 evaluated (as the influence of quartz in metakaolin), so the conclusions of this article cannot be
892 generalized to all alkali-activated binders without precautions being taken.

893

894 This study reveals that each mixture tested had different behaviour depending on the drying
895 temperature. The synthesis in Table 5 allows the optimal drying to be chosen according to the
896 characterization or durability test to be carried out.

897 For geopolymer, the microstructure is damaged for drying temperatures above 40°C but mineralogy
898 does not appear to be affected with our formula. This is linked to an increase in pore size and nano-
899 to microcracking, which is probably linked with shrinkage and a reorganization of the geopolymer
900 paste. For a test linked to the microstructure (e.g. strength, permeability, chloride migration,
901 carbonation) drying at 40°C will therefore be chosen, accepting that part of the water will still be

present in the porosity. On the other hand, for a test related to chemistry or mineralogy, a drying temperature of 105°C will be a good option as it enables more water to be removed.

GGBS activated by silicate or carbonate should be dried at 105°C for most tests, with the exception of those related to porosity, which require inefficient drying at 20°C. Note that drying at 40-60°C in a low humidity environment considerably affects the mechanical strength. This is probably related to desaturation of C-(A)-S-H intercrystallite pores in addition to drying shrinkage. The higher drying rate at higher temperatures might limit the internal mechanical stress and preserve the material.

Finally, Mk-GGBS-silicate combines the drawbacks of geopolymer and GGBS-silicate and both microstructure and mineralogical assemblage seem to be affected regardless of the drying temperature used. However, by using other proportions between the two precursors, more encouraging results can be obtained.

According to the data highlighted in this article, it is not possible to conclude on an optimal drying temperature for all AAMs and all sustainability analyses. To ensure that the preconditioning step has not been too harmful for a sample, it would be wise to always compare mechanical strength (or ultrasonic pulse velocity for geopolymer) on dried and non-dried samples. If a significant difference is observed between the two, it would then be necessary to distinguish the properties inherent in the materials from those induced by preconditioning.

7. References

[1] J. Davidovits, Geopolymers: inorganic polymeric new materials, Journal of Thermal Analysis and Calorimetry. 37 (1991) 1633–1656.

[2] J.L. Provis, J.S.J. van Deventer, Geopolymers: structures, processing, properties and industrial applications, Elsevier, 2009.

927 [3] C. Shi, A.F. Jiménez, A. Palomo, New cements for the 21st century: The pursuit of an
928 alternative to Portland cement, Cement and Concrete Research. 41 (2011) 750–763.
929 https://doi.org/10.1016/j.cemconres.2011.03.016.
930 [4] F. Pacheco-Torgal, J.A. Labrincha, C. Leonelli, A. Palomo, P. Chindaprasirt, Handbook
931 of Alkali-Activated Cements, Mortars and Concretes, Elsevier, 2015.
932 https://doi.org/10.1016/C2013-0-16511-7.
933 [5] S.A. Bernal, J.L. Provis, Durability of alkali-activated materials: progress and
934 perspectives, Journal of the American Ceramic Society. 97 (2014) 997–1008.
935 [6] M.M. Hossain, M.R. Karim, M.K. Hossain, M.N. Islam, M.F.M. Zain, Durability of
936 mortar and concrete containing alkali-activated binder with pozzolans: A review,
937 Construction and Building Materials. 93 (2015) 95–109.
938 https://doi.org/10.1016/j.conbuildmat.2015.05.094.
939 [7] K. Arbi, M. Nedeljković, Y. Zuo, G. Ye, A Review on the Durability of Alkali-Activated
940 Fly Ash/Slag Systems: Advances, Issues, and Perspectives, Ind. Eng. Chem. Res. 55
941 (2016) 5439–5453. https://doi.org/10.1021/acs.iecr.6b00559.
942 [8] J. Zhang, C. Shi, Z. Zhang, Z. Ou, Durability of alkali-activated materials in aggressive
943 environments: A review on recent studies, Construction and Building Materials. 152
944 (2017) 598–613. https://doi.org/10.1016/j.conbuildmat.2017.07.027.
945 [9] T. Luukkonen, Z. Abdollahnejad, J. Yliniemi, P. Kinnunen, M. Illikainen, One-part alkali-
946 activated materials: A review, Cement and Concrete Research. 103 (2018) 21–34.
947 https://doi.org/10.1016/j.cemconres.2017.10.001.
948 [10] I. Ismail, S.A. Bernal, J.L. Provis, S. Hamdan, J.S.J. van Deventer, Drying-induced
949 changes in the structure of alkali-activated pastes, J Mater Sci. 48 (2013) 3566–3577.
950 https://doi.org/10.1007/s10853-013-7152-9.

951 [11] K. Yang, C. Yang, B. Magee, S. Nanukuttan, J. Ye, Establishment of a
952 preconditioning regime for air permeability and sorptivity of alkali-activated slag
953 concrete, Cement and Concrete Composites. 73 (2016) 19–28.
954 https://doi.org/10.1016/j.cemconcomp.2016.06.019.
955 [12] Z. Zhang, Y. Zhu, H. Zhu, Y. Zhang, J.L. Provis, H. Wang, Effect of drying
956 procedures on pore structure and phase evolution of alkali-activated cements, Cement and
957 Concrete Composites. 96 (2019) 194–203.
958 https://doi.org/10.1016/j.cemconcomp.2018.12.003.
959 [13] G.J. Gluth, K. Arbi, S.A. Bernal, D. Bondar, A. Castel, S. Chithiraputhiran, A.
960 Dehghan, K. Dombrowski-Daube, A. Dubey, V. Ducman, RILEM TC 247-DTA round
961 robin test: carbonation and chloride penetration testing of alkali-activated concretes,
962 Materials and Structures. 53 (2020) 1–17.
963 [14] F. Winnefeld, G.J. Gluth, S.A. Bernal, M.C. Bignozzi, L. Carabba, S.
964 Chithiraputhiran, A. Dehghan, S. Dolenec, K. Dombrowski-Daube, A. Dubey, RILEM
965 TC 247-DTA round robin test: sulfate resistance, alkali-silica reaction and freeze–thaw
966 resistance of alkali-activated concretes, Materials and Structures. 53 (2020) 1–17.
967 [15] S.A. Bernal, R. San Nicolas, J.L. Provis, R. Mejía de Gutiérrez, J.S.J. van Deventer,
968 Natural carbonation of aged alkali-activated slag concretes, Mater Struct. 47 (2014) 693–
969 707. https://doi.org/10.1617/s11527-013-0089-2.
970 [16] J.L. Provis, J.S. Van Deventer, eds., Alkali activated materials: State-of-the-art Report,
971 Rilem Tc 224-AAM, Springer, Dordrecht, 2014.
972 [17] M. Kovtun, Effect of Preconditioning on Durability Indices of Alkali-Activated
973 Concretes, SP. 326 (2018) 19.1-19.6.
974 [18] N.C. Collier, J.H. Sharp, N.B. Milestone, J. Hill, I.H. Godfrey, The influence of water
975 removal techniques on the composition and microstructure of hardened cement pastes,

976 Cement and Concrete Research. 38 (2008) 737–744.
977 https://doi.org/10.1016/j.cemconres.2008.02.012.
978 [19] A. Bogner, J. Schatz, F. Dehn, H.S. Müller, Influence of Drying on the Microstructure
979 of Hardened Cement Paste: A Mercury Intrusion Porosimetry, Nitrogen Sorption and
980 SAXS Study, ACT. 18 (2020) 83–94. https://doi.org/10.3151/jact.18.83.
981 [20] C. Gallé, Effect of drying on cement-based materials pore structure as identified by
982 mercury intrusion porosimetry A comparative study between oven-, vacuum-, and freeze-
983 drying, Cement and Concrete Research. (2001) 11.
984 [21] J.J. Beaudoin, A discussion on, "The use of nitrogen adsorption to assess the
985 microstructure of cement paste" by M.C.G. Juenger and H.M. Jennings, Cement and
986 Concrete Research. 32 (2002) 831–832. https://doi.org/10.1016/S0008-8846(01)00742-6.
987 [22] J. Zhang, G.W. Scherer, Comparison of methods for arresting hydration of cement,
988 Cement and Concrete Research. 41 (2011) 1024–1036.
989 https://doi.org/10.1016/j.cemconres.2011.06.003.
990 [23] K.K. Aligizaki, Pore structure of cement-based materials: testing, interpretation and
991 requirements, Taylor & Francis, Abingdon [England] ; New York, 2006.
992 [24] A. Korpa, R. Trettin, The influence of different drying methods on cement paste
993 microstructures as reflected by gas adsorption: Comparison between freeze-drying (F-
994 drying), D-drying, P-drying and oven-drying methods, Cement and Concrete Research. 36
995 (2006) 634–649. https://doi.org/10.1016/j.cemconres.2005.11.021.
996 [25] D. Snoeck, L.F. Velasco, A. Mignon, S. Van Vlierberghe, P. Dubruel, P. Lodewyckx,
997 N. De Belie, The influence of different drying techniques on the water sorption properties
998 of cement-based materials, Cement and Concrete Research. 64 (2014) 54–62.
999 https://doi.org/10.1016/j.cemconres.2014.06.009.

[26] R. Snellings, J. Chwast, Ö. Cizer, N. De Belie, Y. Dhandapani, P. Durdzinski, J. Elsen, J. Haufe, D. Hooton, C. Patapy, M. Santhanam, K. Scrivener, D. Snoeck, L. Steger, S. Tongbo, A. Vollpracht, F. Winnefeld, B. Lothenbach, Report of TC 238-SCM: hydration stoppage methods for phase assemblage studies of blended cements—results of a round robin test, Mater Struct. 51 (2018) 111. https://doi.org/10.1617/s11527-018-1237-5.

[27] Z. Zhang, G.W. Scherer, Evaluation of drying methods by nitrogen adsorption, Cement and Concrete Research. 120 (2019) 13–26. https://doi.org/10.1016/j.cemconres.2019.02.016.

[28] C. Rößler, A. Eberhardt, H. Kučerová, B. Möser, Influence of hydration on the fluidity of normal Portland cement pastes, Cement and Concrete Research. 38 (2008) 897–906. https://doi.org/10.1016/j.cemconres.2008.03.003.

[29] J.J. Beaudoin, P. Gu, J. Marchand, B. Tamtsia, R.E. Myers, Z. Liu, Solvent Replacement Studies of Hydrated Portland Cement Systems: The Role of Calcium Hydroxide, Advanced Cement Based Materials. 8 (1998) 56–65. https://doi.org/10.1016/S1065-7355(98)00008-X.

[30] L. Zhang, F.P. Glasser, Critical examination of drying damage to cement pastes, Advances in Cement Research. 12 (2000) 79–88. https://doi.org/10.1680/adcr.2000.12.2.79.

[31] M. Giroudon, M. Peyre Lavigne, C. Patapy, A. Bertron, Blast-furnace slag cement and metakaolin based geopolymer as construction materials for liquid anaerobic digestion structures: Interactions and biodeterioration mechanisms, Science of The Total Environment. 750 (2021) 141518. https://doi.org/10.1016/j.scitotenv.2020.141518.

[32] R. San Nicolas, M. Cyr, G. Escadeillas, Characteristics and applications of flash metakaolins, Applied Clay Science. 83–84 (2013) 253–262. https://doi.org/10.1016/j.clay.2013.08.036.

[33] R. Pouhet, M. Cyr, Formulation and performance of flash metakaolin geopolymer concretes, Construction and Building Materials. 120 (2016) 150–160. https://doi.org/10.1016/j.conbuildmat.2016.05.061.

[34] R. Pouhet, M. Cyr, R. Bucher, Influence of the initial water content in flash calcined metakaolin-based geopolymer, Construction and Building Materials. 201 (2019) 421–429. https://doi.org/10.1016/j.conbuildmat.2018.12.201.

[35] H. Lahalle, V. Benavent, V. Trincal, T. Wattez, R. Bucher, M. Cyr, Robustness to water and temperature, and activation energies of metakaolin-based geopolymer and alkali-activated slag binders, Construction and Building Materials. 300 (2021) 124066. https://doi.org/10.1016/j.conbuildmat.2021.124066.

[36] H.C. Hardy, D. Telfair, W.H. Pielemeier, The Velocity of Sound in Air, The Journal of the Acoustical Society of America. 13 (1942) 9. https://doi.org/doi: 10.1121/1.1916169.

[37] S.W. Kieffer, Sound speed in liquid-gas mixtures: Water-air and water-steam, J. Geophys. Res. 82 (1977) 2895–2904. https://doi.org/10.1029/JB082i020p02895.

[38] A. Quiviger, Ultrasons diffus pour la caractérisation d'une fissure dans le béton.: approche linéaire et non linéaire., PhD Thesis, Aix-Marseille, 2012.

[39] M.G. Hernández, M.A.G. Izquierdo, A. Ibáñez, J.J. Anaya, L.G. Ullate, Porosity estimation of concrete by ultrasonic NDE, Ultrasonics. 38 (2000) 531–533. https://doi.org/10.1016/S0041-624X(99)00095-5.

[40] Z. Lafhaj, M. Goueygou, A. Djerbi, M. Kaczmarek, Correlation between porosity, permeability and ultrasonic parameters of mortar with variable water/cement ratio and water content, Cement and Concrete Research. 36 (2006) 625–633. https://doi.org/10.1016/j.cemconres.2005.11.009.

[41] N. Toubal Seghir, O. Benaimeche, K. Krzywiński, Ł. Sadowski, Ultrasonic Evaluation of Cement-Based Building Materials Modified Using Marble Powder Sourced from Industrial Wastes, Buildings. 10 (2020) 38. https://doi.org/10.3390/buildings10030038.

[42] J. Zhu, S.-H. Kee, D. Han, Y.-T. Tsai, Effects of air voids on ultrasonic wave propagation in early age cement pastes, Cement and Concrete Research. 41 (2011) 872–881. https://doi.org/10.1016/j.cemconres.2011.04.005.

[43] E. Ohdaira, N. Masuzawa, Water content and its effect on ultrasound propagation in concrete — the possibility of NDE, Ultrasonics. 38 (2000) 546–552. https://doi.org/10.1016/S0041-624X(99)00158-4.

[44] T.P. Philippidis, D.G. Aggelis, Experimental study of wave dispersion and attenuation in concrete, Ultrasonics. 43 (2005) 584–595. https://doi.org/10.1016/j.ultras.2004.12.001.

[45] W. Wang, C. Lu, G. Yuan, Y. Zhang, Effects of pore water saturation on the mechanical properties of fly ash concrete, Construction and Building Materials. 130 (2017) 54–63. https://doi.org/10.1016/j.conbuildmat.2016.11.031.

[46] Ma.D.E. Candelaria, S.-H. Kee, J.-J. Yee, J.-W. Lee, Effects of Saturation Levels on the Ultrasonic Pulse Velocities and Mechanical Properties of Concrete, Materials. 14 (2021) 152. https://doi.org/10.3390/ma14010152.

[47] F. Saint-Pierre, A. Philibert, B. Giroux, P. Rivard, Concrete Quality Designation based on Ultrasonic Pulse Velocity, Construction and Building Materials. 125 (2016) 1022–1027. https://doi.org/10.1016/j.conbuildmat.2016.08.158.

[48] S. Hong, S. Yoon, J. Kim, C. Lee, S. Kim, Y. Lee, Evaluation of Condition of Concrete Structures Using Ultrasonic Pulse Velocity Method, Applied Sciences. 10 (2020) 19.

1072 [49] S. Ould Naffa, M. Goueygou, B. Piwakowski, F. Buyle-Bodin, Detection of chemical
1073 damage in concrete using ultrasound, Ultrasonics. 40 (2002) 247–251.
1074 https://doi.org/10.1016/S0041-624X(02)00146-4.
1075 [50] F. Saint-Pierre, P. Rivard, G. Ballivy, Measurement of alkali–silica reaction
1076 progression by ultrasonic waves attenuation, Cement and Concrete Research. 37 (2007)
1077 948–956. https://doi.org/10.1016/j.cemconres.2007.02.022.
1078 [51] D.A. Bohn, Environmental effects on the speed of sound, in: Audio Engineering
1079 Society Convention 83, Audio Engineering Society, 1987.
1080 [52] G. Ye, P. Lura, K. van Breugel, A.L.A. Fraaij, Study on the development of the
1081 microstructure in cement-based materials by means of numerical simulation and
1082 ultrasonic pulse velocity measurement, Cement and Concrete Composites. 26 (2004) 491–
1083 497. https://doi.org/10.1016/S0958-9465(03)00081-7.
1084 [53] J. Berriman, P. Purnell, D.A. Hutchins, A. Neild, Humidity and aggregate content
1085 correction factors for air-coupled ultrasonic evaluation of concrete, Ultrasonics. 43 (2005)
1086 211–217. https://doi.org/10.1016/j.ultras.2004.07.003.
1087 [54] W. López, J.A. González, Influence of the degree of pore saturation on the resistivity
1088 of concrete and the corrosion rate of steel reinforcement, Cement and Concrete Research.
1089 23 (1993) 368–376. https://doi.org/10.1016/0008-8846(93)90102-F.
1090 [55] P. Rivard, F. Saint-Pierre, Assessing alkali-silica reaction damage to concrete with
1091 non-destructive methods: From the lab to the field, Construction and Building Materials.
1092 23 (2009) 902–909. https://doi.org/10.1016/j.conbuildmat.2008.04.013.
1093 [56] P.J. Tumidajski, A.S. Schumacher, S. Perron, P. Gu, J.J. Beaudoin, On the relationship
1094 between porosity and electrical resistivity in cementitious systems, Cement and Concrete
1095 Research. 26 (1996) 539–544. https://doi.org/10.1016/0008-8846(96)00017-8.
1096 [57] E.W. Washburn, The dynamics of capillary flow, Physical Review. 17 (1921) 273.

[58] Micromeritics, AutoPore IV 9500 - Operator's Manual Rev A - 950-42801-01, 2015.

[59] M. Gasc-Barbier, S. Chanchole, De l'utilisation d'échantillons humides en porosimétrie au mercure, Revue Française de Géotechnique. (2005) 7.

[60] M. Staněk, Y. Géraud, Granite microporosity changes due to fracturing and alteration: secondary mineral phases as proxies for porosity and permeability estimation, Solid Earth. 10 (2019) 251–274. https://doi.org/10.5194/se-10-251-2019.

[61] J.M. Ortega, M. Cabeza, A.J. Tenza-Abril, T. Real-Herraiz, M.Á. Climent, I. Sánchez, Effects of red mud addition in the microstructure, durability and mechanical performance of cement mortars, Applied Sciences. 9 (2019) 984.

[62] M. Thiery, Modelling of atmospheric carbonation of cement based materials considering the kinetic effects and modifications of the microstructure and the hydric state, PhD Thesis, Ecole des Ponts ParisTech, 2005.

[63] S. Stephant, Étude de l'influence de l'hydratation des laitiers sur les propriétés de transfert gazeux dans les matériaux cimentaires, PhD Thesis, Université de Bourgogne, 2015. http://rgdoi.net/10.13140/RG.2.1.1665.4483.

[64] R.L. Portsmouth, L.F. Gladden, Determination of pore connectivity by mercury porosimetry, Chemical Engineering Science. 46 (1991) 3023–3036. https://doi.org/10.1016/0009-2509(91)85006-J.

[65] V.G. Mata, J.C.B. Lopes, M.M. Dias, Porous media characterization using mercury porosimetry simulation. 1. Description of the simulator and its sensitivity to model parameters, Industrial & Engineering Chemistry Research. 40 (2001) 3511–3522.

[66] V.G. Mata, J.C.B. Lopes, M.M. Dias, Porous media characterization using mercury porosimetry simulation. 2. An iterative method for the determination of the real pore size distribution and the mean coordination number, Industrial & Engineering Chemistry Research. 40 (2001) 4836–4843.

[67] V. Trincal, D. Charpentier, M.D. Buatier, B. Grobety, B. Lacroix, P. Labaume, J.-P. Sizun, Quantification of mass transfers and mineralogical transformations in a thrust fault (Monte Perdido thrust unit, southern Pyrenees, Spain), Marine and Petroleum Geology. 55 (2014) 160–175. https://doi.org/10.1016/j.marpetgeo.2013.12.016.

[68] J.L. Kulp, P. Kent, P.F. Kerr, Thermal study of the Ca-Mg-Fe carbonate minerals, American Mineralogist. 36 (1951) 643–670.

[69] M. Földvári, Handbook of thermogravimetric system of minerals and its use in geological practice, 2011. https://geo-portal.hu/sites/default/files/files/K%C3%B6nyvtar/Alkalmi_teljes/Fodvari_egyben.pdf.

[70] W. Thomson, On the Equilibrium of Vapour at a Curved Surface of Liquid, Proc. R. Soc. Edinb. 7 (1872) 63–68. https://doi.org/10.1017/S0370164600041729.

[71] H. Ye, A. Radlińska, A review and comparative study of existing shrinkage prediction models for portland and non-portland cementitious materials, Advances in Materials Science and Engineering. 2016 (2016).

[72] V. Benavent, Caractérisation de la porosité des géopolymères: évolution temporelle et étude de l'eau confinée, PhD Thesis, Montpellier, 2016.

[73] P. Duxson, G.C. Lukey, J.S. van Deventer, Physical evolution of Na-geopolymer derived from metakaolin up to 1000 C, Journal of Materials Science. 42 (2007) 3044–3054.

[74] J. Rouyer, V. Benavent, F. Frizon, A. Poulesquen, Influence of geopolymer formulation parameters on the elastic and porous properties over a one-year monitoring, Materials Letters. 207 (2017) 121–124. https://doi.org/10.1016/j.matlet.2017.06.125.

[75] S.J. Barnett, M.N. Soutsos, S.G. Millard, J.H. Bungey, Strength development of mortars containing ground granulated blast-furnace slag: Effect of curing temperature and

determination of apparent activation energies, Cement and Concrete Research. 36 (2006) 434–440. https://doi.org/10.1016/j.cemconres.2005.11.002.

[76] F. Sajedi, H.A. Razak, Comparison of different methods for activation of ordinary Portland cement-slag mortars, Construction and Building Materials. 25 (2011) 30–38. https://doi.org/10.1016/j.conbuildmat.2010.06.060.

[77] P. Azar, G. Samson, F. Deby, H. Lahalle, V. Benavent, M. Cyr, Chloride-induced corrosion in ordinary and alkali-activated concrete, (2020) 20.

[78] S. Diamond, A discussion of the paper "Effect of drying on cement-based materials pore structure as identified by mercury porosimetry—a comparative study between oven-, vacuum-, and freeze-drying" by C. Gallé, Cement and Concrete Research. 33 (2003) 169–170. https://doi.org/10.1016/S0008-8846(02)00940-7.

[79] V. Benavent, F. Frizon, A. Poulesquen, Effect of composition and aging on the porous structure of metakaolin-based geopolymers, Journal of Applied Crystallography. 49 (2016) 2116–2128. https://doi.org/10.1107/S1600576716014618.

[80] V. Thiéry, V. Trincal, C.A. Davy, The elusive ettringite under the high-vacuum SEM – a reflection based on natural samples, the use of Monte Carlo modelling of EDS analyses and an extension to the ettringite group minerals, Journal of Microscopy. (2017) n/a-n/a. https://doi.org/10.1111/jmi.12589.

[81] K.O. Kjellsen, H.M. Jennings, Observations of microcracking in cement paste upon drying and rewetting by environmental scanning electron microscopy, Advanced Cement Based Materials. 3 (1996) 14–19.

[82] S.A. Bernal, J.L. Provis, V. Rose, R.M. De Gutierrez, Evolution of binder structure in sodium silicate-activated slag-metakaolin blends, Cement and Concrete Composites. 33 (2011) 46–54.

[83] M. Criado, A. Palomo, A. Fernandezjimenez, Alkali activation of fly ashes. Part 1: Effect of curing conditions on the carbonation of the reaction products, Fuel. 84 (2005) 2048–2054. https://doi.org/10.1016/j.fuel.2005.03.030.

[84] X. Guo, H. Shi, Metakaolin-, fly ash-and calcium hydroxide-based geopolymers: effects of calcium on performance, Advances in Cement Research. 27 (2015) 559–566.

[85] M. Król, J. Minkiewicz, W. Mozgawa, IR spectroscopy studies of zeolites in geopolymeric materials derived from kaolinite, Journal of Molecular Structure. 1126 (2016) 200–206.

[86] M.A. Villaquirán-Caicedo, R.M. de Gutiérrez, S. Sulekar, C. Davis, J.C. Nino, Thermal properties of novel binary geopolymers based on metakaolin and alternative silica sources, Applied Clay Science. 118 (2015) 276–282.

[87] M.R. Rowles, J.V. Hanna, K.J. Pike, M.E. Smith, B.H. O'Connor, 29Si, 27Al, 1H and 23Na MAS NMR Study of the Bonding Character in Aluminosilicate Inorganic Polymers, Appl Magn Reson. 32 (2007) 663–689. https://doi.org/10.1007/s00723-007-0043-y.

[88] Q.H. Nguyen, M. Hanafi, J. Merkl, J.-B. d'Espinose de Lacaillerie, Evolution of the microstructure of unconsolidated geopolymers by thermoporometry, Journal of the American Ceramic Society. 104 (2021) 1581–1591.

[89] M.J. DeJong, F.-J. Ulm, The nanogranular behavior of CSH at elevated temperatures (up to 700 C), Cement and Concrete Research. 37 (2007) 1–12.

[90] E.T. Rodriguez, K. Garbev, D. Merz, L. Black, I.G. Richardson, Thermal stability of CSH phases and applicability of Richardson and Groves' and Richardson C-(A)-SH (I) models to synthetic CSH, Cement and Concrete Research. 93 (2017) 45–56.

[91] Y. He, X. Zheng, L. Lü, S. Yu, G. Deng, S. Hu, Dehydration Characteristics of CSH with Ca/Si Ratio 1.0 Prepared Via Precipitation, Journal of Wuhan University of Technology-Mater. Sci. Ed. 33 (2018) 619–624.

[92] A. Abdalqader, F. Jin, A. Al-Tabbaa, Performance of magnesia-modified sodium carbonate-activated slag/fly ash concrete, Cement and Concrete Composites. 103 (2019) 160–174.

[93] R.R. Lloyd, The durability of inorganic polymer cements, PhD Thesis, 2008.

[94] C. Kuenzel, L.J. Vandeperre, S. Donatello, A.R. Boccaccini, C. Cheeseman, Ambient temperature drying shrinkage and cracking in metakaolin-based geopolymers, Journal of the American Ceramic Society. 95 (2012) 3270–3277.

[95] P. Gao, Effect of relative humidity on drying-induced damage in concrete: A comparative study of digital image correlation and lattice modelling, Materials and Design. (2020) 17.

[96] H. Ye, C. Cartwright, F. Rajabipour, A. Radlińska, Effect of drying rate on shrinkage of alkali-activated slag cements, (2014).

[97] Z. Jia, Y. Yang, L. Yang, Y. Zhang, Z. Sun, Hydration products, internal relative humidity and drying shrinkage of alkali activated slag mortar with expansion agents, Construction and Building Materials. 158 (2018) 198–207. https://doi.org/10.1016/j.conbuildmat.2017.09.162.

[98] M. Daimon, S.A. Abo-El-Enein, G. Hosaka, S. Goto, Pore Structure of Calcium Silicate Hydrate in Hydrated Tricalcium Silicate, 60 (1977) 5.

[99] A. Plassais, Nanoporosité, texture et propriétés mécaniques de pâtes de ciments, PhD Thesis, Université Pierre et Marie Curie, 2003.

[100] Y. Aono, F. Matsushita, S. Shibata, Y. Hama, Nano-structural Changes of C-S-H in Hardened Cement Paste during Drying at 50°C, ACT. 5 (2007) 313–323. https://doi.org/10.3151/jact.5.313.

[101] M. Hojati, F. Rajabipour, A. Radlińska, Drying shrinkage of alkali-activated cements: effect of humidity and curing temperature, Mater Struct. 52 (2019) 118. https://doi.org/10.1617/s11527-019-1430-1.

[102] H. Ye, A. Radlińska, Shrinkage mechanisms of alkali-activated slag, Cement and Concrete Research. 88 (2016) 126–135.

[103] H. Ye, C. Cartwright, F. Rajabipour, A. Radlińska, Understanding the drying shrinkage performance of alkali-activated slag mortars, Cement and Concrete Composites. 76 (2017) 13–24. https://doi.org/10.1016/j.cemconcomp.2016.11.010.

[104] Z. Li, G. Ye, Experimental study of the chemical deformation of metakaolin based geopolymer, Proceedings of the SynerCrete. 18 (2018).

[105] S. Blotevogel, A. Ehrenberg, L. Steger, L. Doussang, J. Kaknics, C. Patapy, M. Cyr, Ability of the R3 test to evaluate differences in early age reactivity of 16 industrial ground granulated blast furnace slags (GGBS), Cement and Concrete Research. 130 (2020) 105998.

[106] S. Blotevogel, L. Steger, D. Hart, L. Doussang, J. Kaknics, M. Poirier, H. Bornhöft, J. Deubener, C. Patapy, M. Cyr, Effect of TiO2 and 11 minor elements on the reactivity of ground-granulated blast-furnace slag in blended cements, Journal of the American Ceramic Society. 104 (2021) 128–139.

[107] T.C. Rilem, 116-PCD. Permeability of concrete as a criterion of its durability, Materials and Structures. 32 (1999) 174–179.

[108] L. Konecny, S.J. Naqvi, The effect of different drying techniques on the pore size distribution of blended cement mortars, Cement and Concrete Research. 23 (1993) 1223–1228. https://doi.org/10.1016/0008-8846(93)90183-A.

[109] L.D. Mitchell, J.C. Margeson, The effects of solvents on C–S–H as determined by thermal analysis, J Therm Anal Calorim. 86 (2006) 591–594. https://doi.org/10.1007/s10973-006-7712-1.

[110] Z. Zhang, G.W. Scherer, Supercritical drying of cementitious materials, Cement and Concrete Research. 99 (2017) 137–154. https://doi.org/10.1016/j.cemconres.2017.05.005.

[111] G.W. Scherer, Stress and strain during supercritical drying, J Sol-Gel Sci Technol. 90 (2019) 8–19. https://doi.org/10.1007/s10971-018-4808-6.

AFPC–AFREM (1997) Détermination de la masse volumique apparente et de la porosité accessible à l'eau, Méthodes recommandées pour la mesure des grandeurs associées à la durabilité. In Compte-rendu des Journées Techniques pp. 121–124. Toulouse.

AS 1012 (1999) Methods of Testing Concrete Method 21: Determination of water absorption and apparent volume of permeable voids in hardened concrete.

ASTM C642 (2006) Standard test method for density, absorption, and voids in hardened concrete.

ASTM C1585 (2011) Standard test method for measurement of rate of absorption of water by hydraulic cement concretes.

ISO 15901-1 (2005) Evaluation of pore size distribution and porosimetry of solid materials by mercury porosimetry and gas adsorption – Part1: Mercury porosimetry. 26p.

ISO 1920-7 (2004) Testing of concrete - Part 7: Non-destructive tests on hardened concrete. 11p.

NF EN 196-1 (2016) Methods of testing cement – Part 1 : Determination of strength. P15-471-1. 38p.

NF EN 197-1 (2012) Cement - Part 1: Composition, spécifications et critères de conformité des ciments courants. Specifications and Conformity Criteria for Common Cements.

NF EN 12390-2 (2019) Testing hardened concrete - Part 2: Making and curing specimens for strength tests. AFNOR 9p.

NF EN 12504-4 (2005) Testing concrete – Part 4: Determination of ultrasonic pulse velocity. P18-447. 17p.

NF EN 13057 (2002) Products and systems for the protection and repair of concrete structures – Test methods – Determination of resistance of capillary absorption. P18-945. 13p.

NF P 18-459 (2010) Concrete – Testing hardened concrete – Testing porosity and density. P18-459. 9p.

SIA 262/1 (2013) Concrete Structures – Supplementary specifications p. 52. Société suisse des ingénieurs.

XP P 18-458 (2008) Tests for hardened concrete – Accelerated carbonation test – Measurement of the thickness of carbonated concrete. P18-458. 12p.

XP P 18-463 (2011) Concrete – Testing gas permeability on hardened concrete. P18-463. 7p.

Acknowledgments

The authors would like to thank Marc Begue, engineer at INSA Toulouse, who helped set up the porosimetry tests and Guillaume Lambare, assistant engineer at UPS Toulouse, for his contribution to TGA analyses. Thanks also to the technician Rémi Pradier, who actively contributed to the project for 6 months. This work is part of the L2A chair (alkali-activated binders) grouping industrial partners EDF, VINCI Construction, ECOCEM Group, ARGECO Développement, VICAT and MBCC Group with the LMDC research laboratory.

Figure captions

Figure 1: Mortar mass monitoring during drying at different temperatures of the geopolymer (a), GGBS-silicate (b), GGBS-carbonate (c), Mk-GGBS-silicate (d), CEM I (e) and CEM III/B (f). For each temperature, data from at least four AAM specimens are superimposed on the figure, while there

1292 are only two samples for Portland cement-based binders. Large dots correspond to the end of drying
1293 (including an additional safety margin of one week) and therefore the age used for the
1294 physicochemical analyses.

1295

1296 **Figure 2:** Water content Vw (wt%) of mortars at the end of drying, obtained by subtracting the mass
1297 change due to conditioning (assumed to be water only) from the mixing water.

1298

1299 **Figure 3:** Compressive strengths (f_c) of mortars cured in autogenous conditions (black spots) or dried
1300 at different temperatures (after autogenous treatment of 28 days). Geopolymer (a), GGBS-silicate
1301 (b), GGBS-carbonate (c), Mk-GGBS-silicate (d), CEM I (e) and CEM III/B (f). Each point corresponds to
1302 the average of three analyses carried out on a 4x4x16 cm^3 sample and given in Supplementary data
1303 A.

1304

1305 **Figure 4:** Mortars pore size distribution for autogenous and dried of geopolymer (a-b), GGBS-silicate
1306 (c-d), GGBS-carbonate (e-f) and Mk-GGBS-silicate (g-h). Autogenous column in dried conditions
1307 graphs represents the average of the samples stored under autogenous conditions and analysed at
1308 different ages (28 to 88 days).

1309

1310 **Figure 5:** SEM backscattered observation of autogenous and dried AAM. Geopolymer dried for 14
1311 days at 40°C (a) or at 105°C (b); GGBS-silicate cured 88 days in autogenous conditions (c) or dried for
1312 35 days at 40°C (d); GGBS-carbonate dried for 35 days at 40°C (e) or 14 days at 105°C (f); Mk-GGBS-
1313 silicate cured for 88 days in autogenous conditions (g) or dried for 24 days at 60°C. More SEM
1314 pictures are given in Supplementary data BS6.

Figure 6: X-ray diffractograms obtained on crushed pastes of geopolymer (A), GGBS-silicate (B), GGBS-carbonate (C) and Mk-GGBS-silicate (D).

Figure 7: Representative FTIR normalized spectra obtained on crushed pastes of geopolymer (a), GGBS-silicate (b), GGBS-carbonate (c) and Mk-GGBS-silicate (d) cured at 20°C in autogenous conditions then dried at different temperatures.

Figure 8: Thermogravimetric analyses measured from room temperature to 1050°C performed on crushed pastes of geopolymer (a), GGBS-silicate (b), GGBS-carbonate (c) and Mk-GGBS-silicate (d).

Figure 9: Drying impact versus temperature for different AAM mixtures, evaluated on (a) Evaporated water, (b) Compressive strength, (c) Ultrasonic pulse velocity, (d) MIP porosity and (e) Pore diameter at half of the main intrusion peak intruded volume (d_{Hm1}). The legend is given in a), 20°C corresponds to 20°C – 50%RH. Removed water was calculated by comparing the loss of mass with the quantity of mixing water. Relative strength and velocity were calculated by comparing samples after drying with the sample of the same age cured in autogenous conditions. The abscissa Endo in ϕ and d_{Hm1} graphs corresponds to the mean of all autogenous samples. The error bars were calculated with a 95% confidence interval.

Table captions

Table 1: Chemical composition in wt% of raw materials obtained with ICP-OES. LOI = loss on ignition.

Table 2: Mineralogical composition of the metakaolin, estimated by Rietveld calculation on X-ray diffractograms following rules described in Trincal et al. [67].

Table 3: Mix-designs of the alkali-activated mortars. Units: masses in grams, w/b in %, density in $g.cm^{-3}$.

Table 4: MIP porosity (φ) in %, degree of pore connectivity (α) in %, and pore diameter (d_{Hm1}) in nm, corresponding to half of the mercury volume intruded in the main intrusion peak; obtained by MIP measurements for geopolymer, GGBS-silicate, GGBS-carbonate and Mk-GGBS-silicate after preconditioning.

Table 5: Drying synthesis.

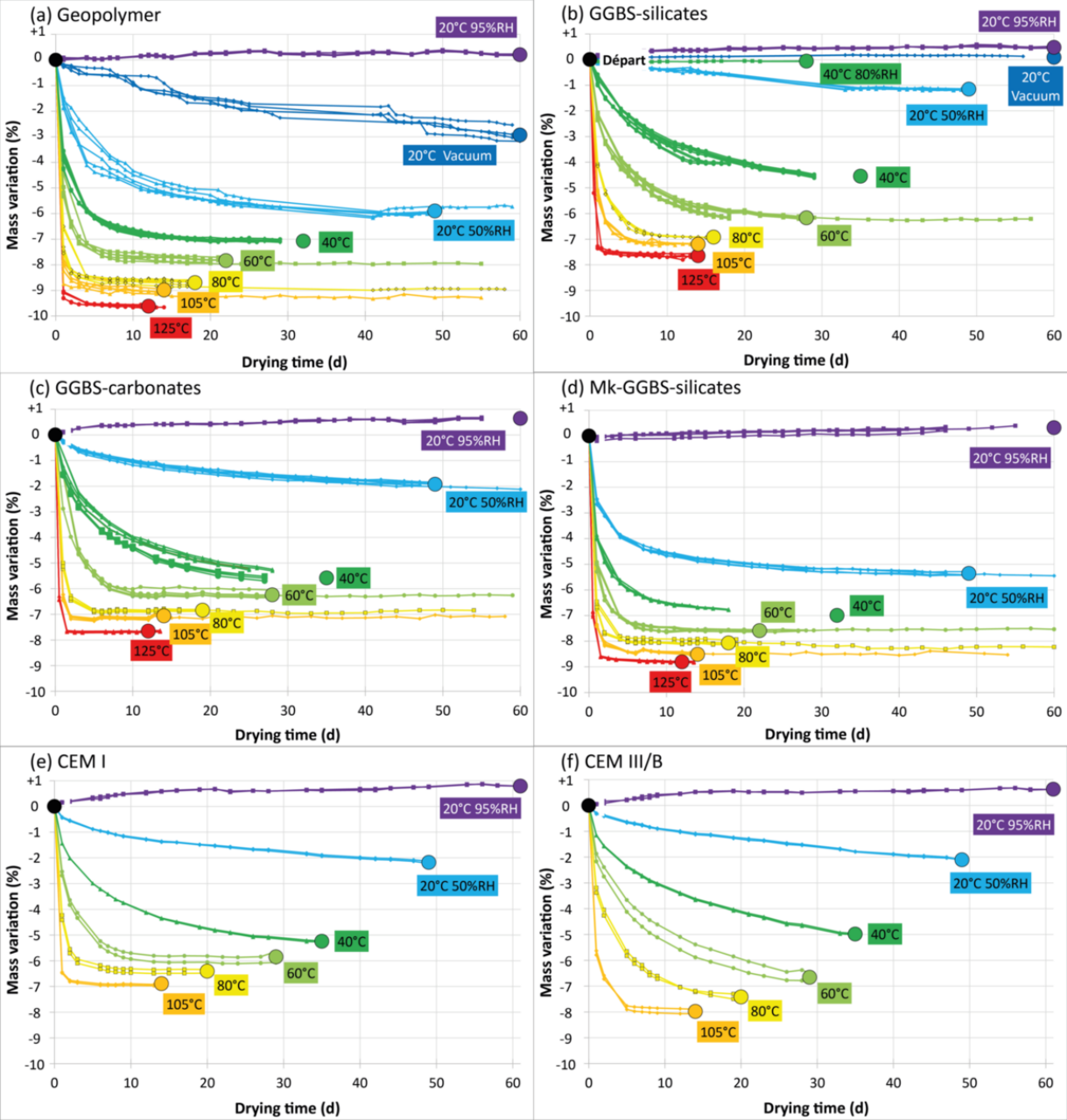
(a) Geopolymer
(b) GGBS-silicates
(c) GGBS-carbonates
(d) Mk-GGBS-silicates
(e) CEM I
(f) CEM III/B
Mass variation (%)
Drying time (d)
Départ
20°C 95%RH
20°C 50%RH
20°C Vacuum
40°C 80%RH
40°C
60°C
80°C
105°C
125°C

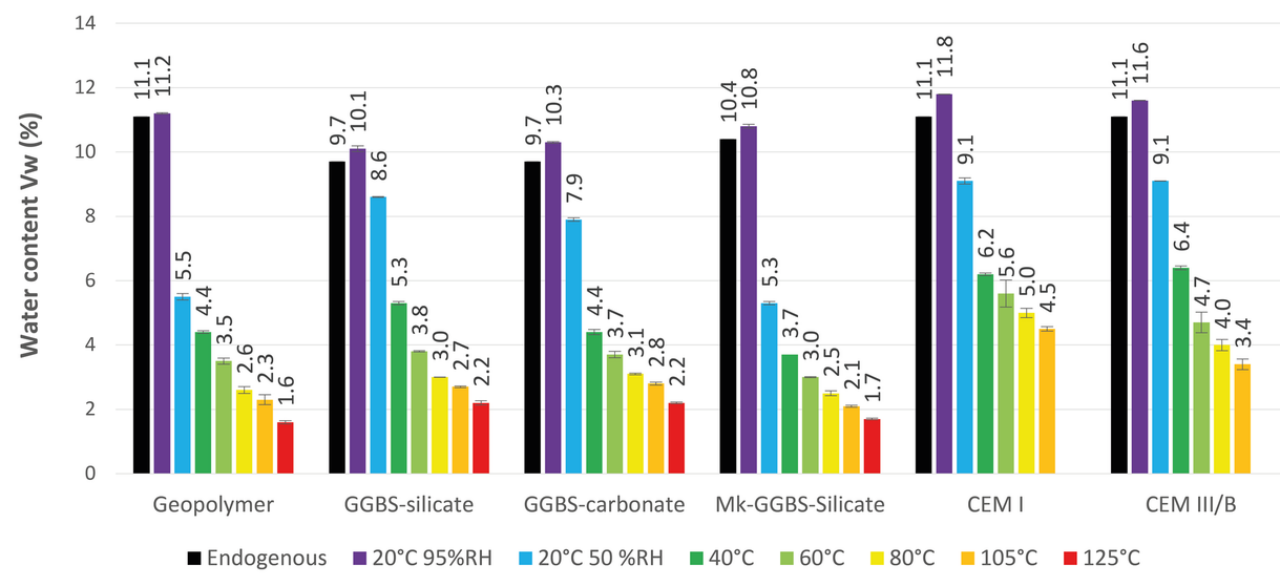
Water content Vw (%)
14
12
10
8
6
4
2
0
11.1
11.2
5.5
4.4
3.5
2.6
2.3
1.6
9.7
10.1
8.6
5.3
3.8
3.0
2.7
2.2
9.7
10.3
7.9
4.4
3.7
3.1
2.8
2.2
10.4
10.8
5.3
3.7
3.0
2.5
2.1
1.7
11.1
11.8
9.1
6.2
5.6
5.0
4.5
11.1
11.6
9.1
6.4
4.7
4.0
3.4
Geopolymer
GGBS-silicate
GGBS-carbonate
Mk-GGBS-Silicate
CEM I
CEM III/B
Endogenous
20°C 95%RH
20°C 50 %RH
40°C
60°C
80°C
105°C
125°C

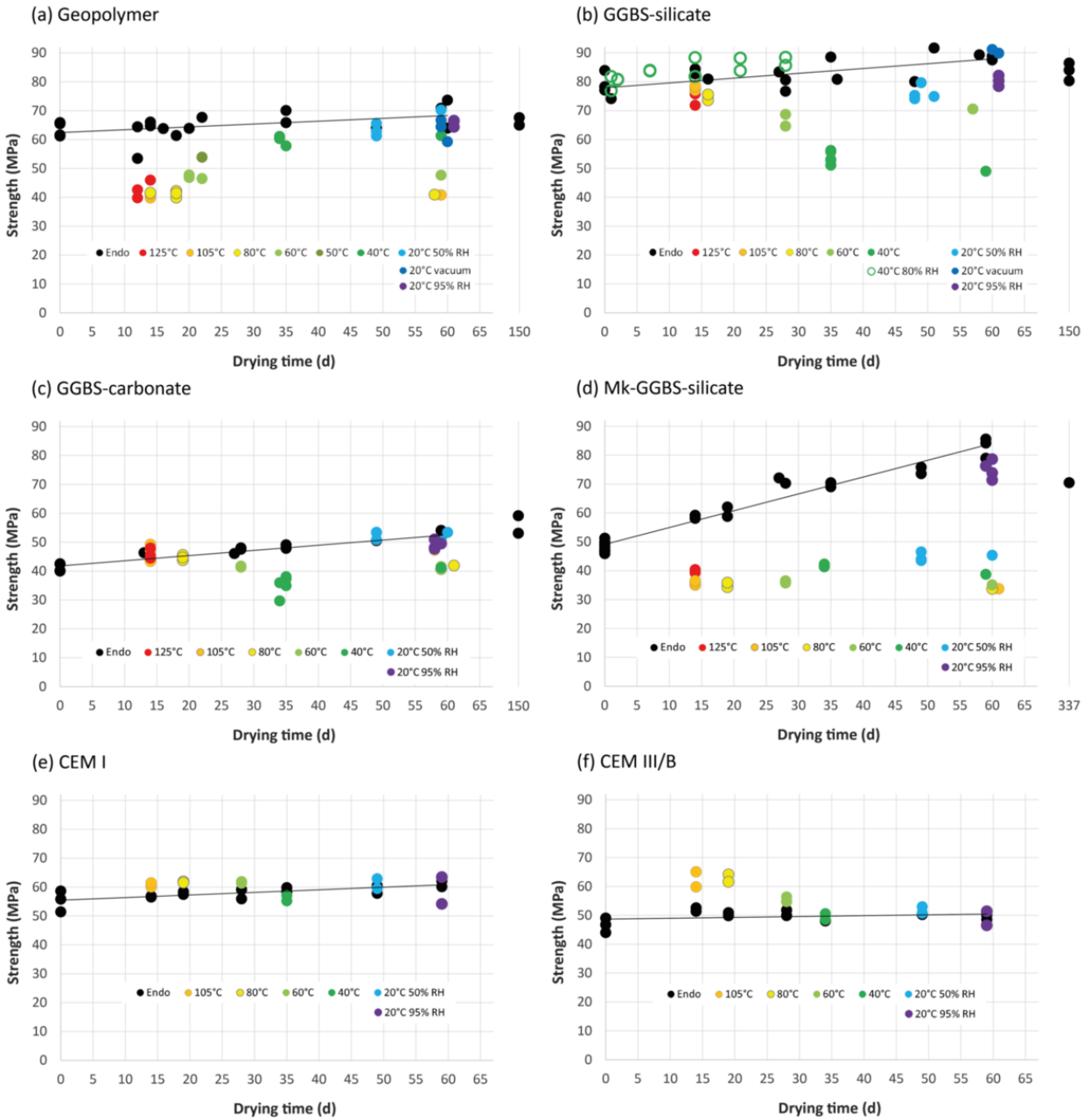
(a) Geopolymer
(b) GGBS-silicate
(c) GGBS-carbonate
(d) Mk-GGBS-silicate
(e) CEM I
(f) CEM III/B
Strength (MPa)
Drying time (d)
Endo
125°C
105°C
80°C
60°C
50°C
40°C
20°C 50% RH
20°C vacuum
20°C 95% RH
40°C 80% RH

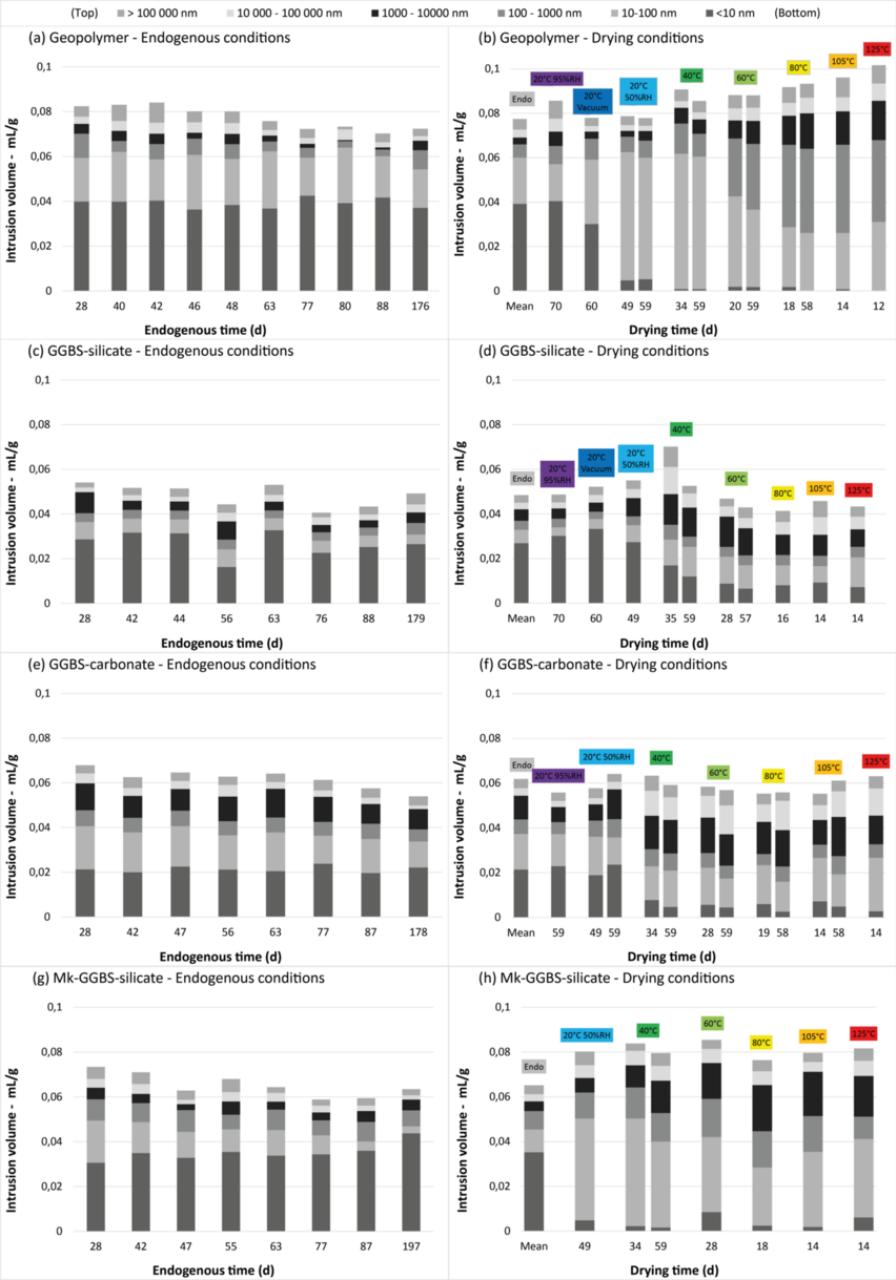
(Top) > 100 000 nm 10 000 - 100 000 nm 1000 - 10000 nm 100 - 1000 nm 10-100 nm <10 nm (Bottom)
(a) Geopolymer - Endogenous conditions
Intrusion volume - mL/g
0,1
0,08
0,06
0,04
0,02
0
28 40 42 46 48 63 77 80 88 176
Endogenous time (d)
(b) Geopolymer - Drying conditions
Endo
20°C 95%RH
20°C Vacuum
20°C 50%RH
40°C
60°C
80°C
105°C
125°C
Mean 70 60 49 59 34 59 20 59 18 58 14 12
Drying time (d)
(c) GGBS-silicate - Endogenous conditions
28 42 44 56 63 76 88 179
Endogenous time (d)
(d) GGBS-silicate - Drying conditions
Mean 70 60 49 35 59 28 57 16 14 14
Drying time (d)
(e) GGBS-carbonate - Endogenous conditions
28 42 47 56 63 77 87 178
Endogenous time (d)
(f) GGBS-carbonate - Drying conditions
Mean 59 49 59 34 59 28 59 19 58 14 58 14
Drying time (d)
(g) Mk-GGBS-silicate - Endogenous conditions
28 42 47 55 63 77 87 197
Endogenous time (d)
(h) Mk-GGBS-silicate - Drying conditions
Mean 49 34 59 28 18 14 14
Drying time (d)

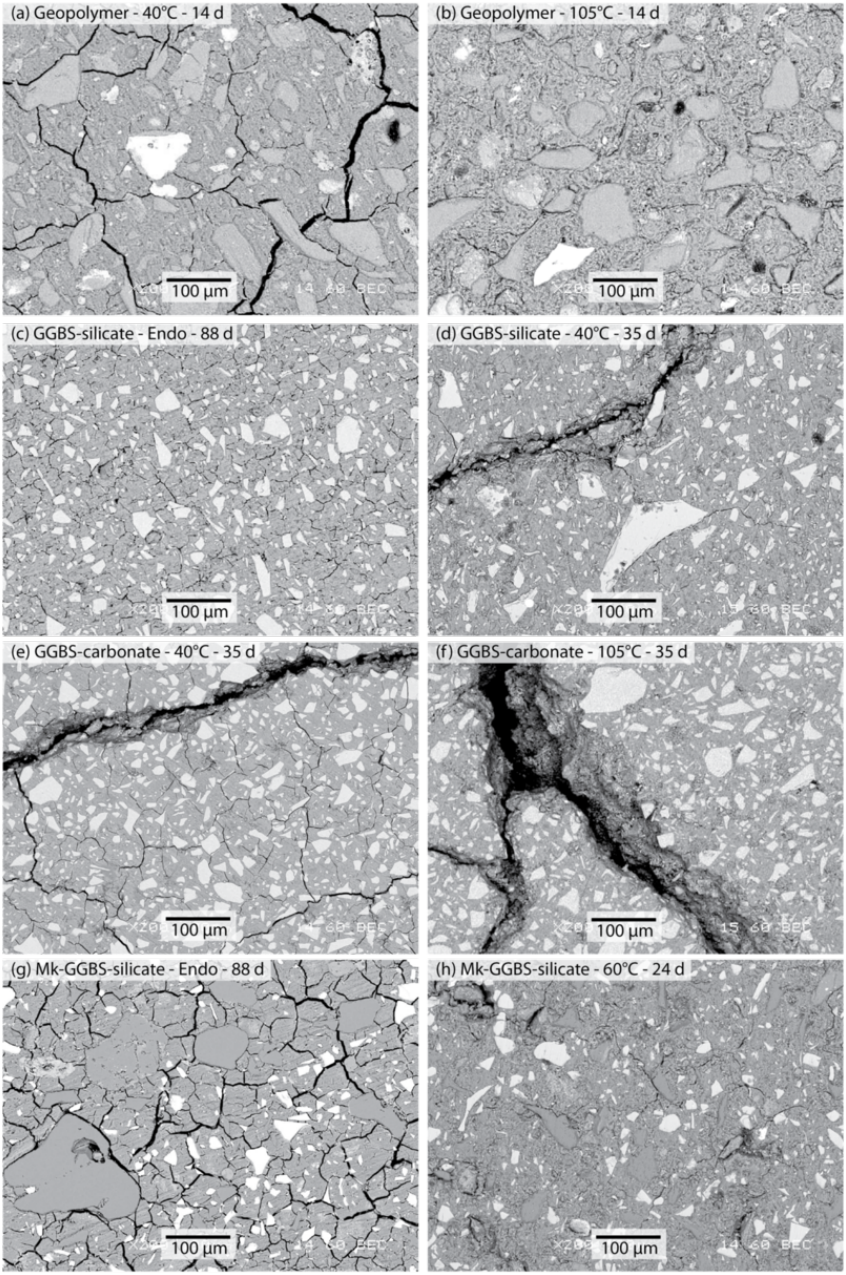
(a) Geopolymer - 40°C - 14 d
100 µm
(b) Geopolymer - 105°C - 14 d
100 µm
(c) GGBS-silicate - Endo - 88 d
100 µm
(d) GGBS-silicate - 40°C - 35 d
100 µm
(e) GGBS-carbonate - 40°C - 35 d
100 µm
(f) GGBS-carbonate - 105°C - 35 d
100 µm
(g) Mk-GGBS-silicate - Endo - 88 d
100 µm
(h) Mk-GGBS-silicate - 60°C - 24 d
100 µm

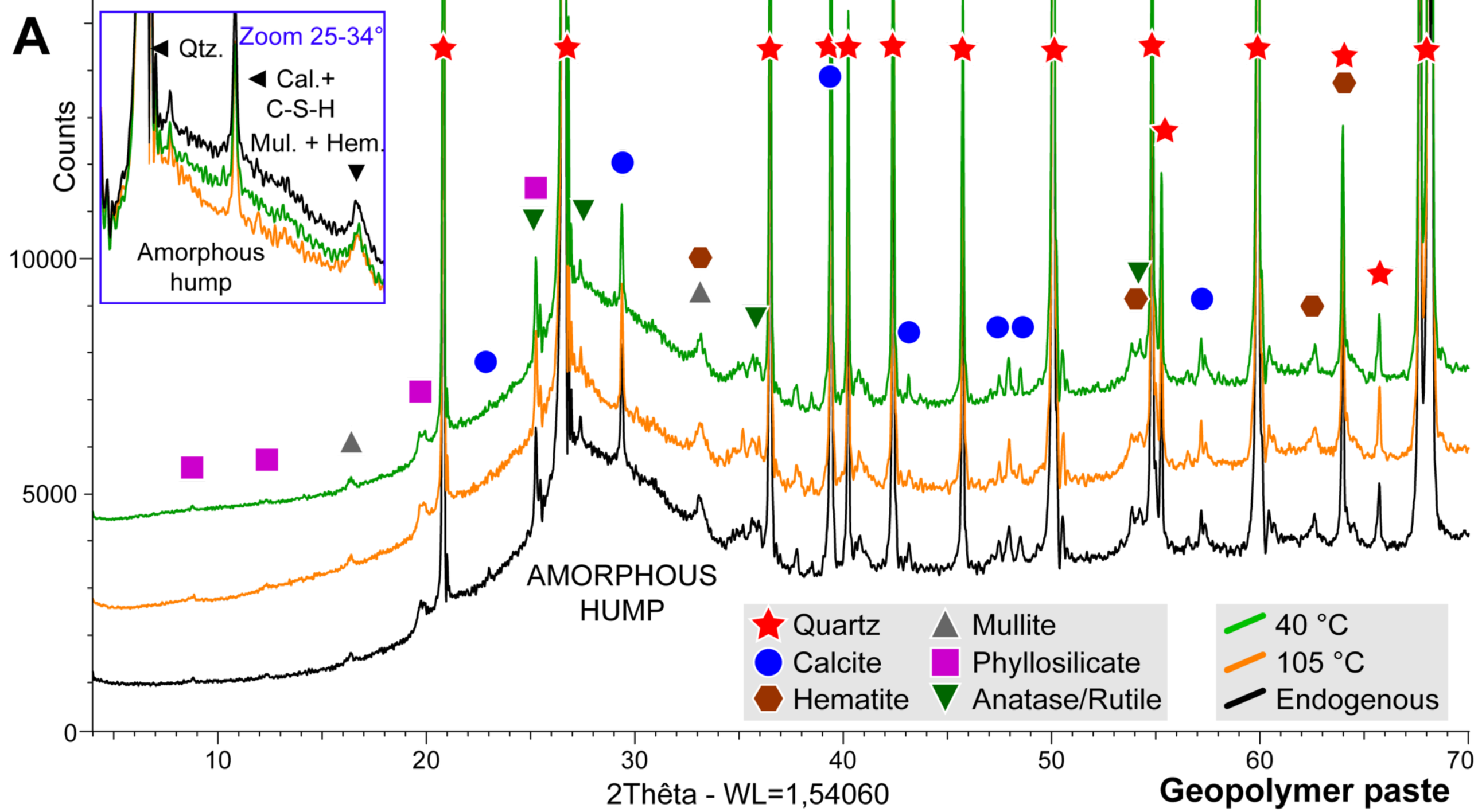
A
Zoom 25-34°
Qtz.
Cal.+
C-S-H
Mul. + Hem.
Amorphous
hump
Counts
10000
5000
0
AMORPHOUS
HUMP
Quartz
Calcite
Hematite
Mullite
Phyllosilicate
Anatase/Rutile
40 °C
105 °C
Endogenous
10
20
30
40
50
60
70
2Thêta - WL=1,54060
Geopolymer paste

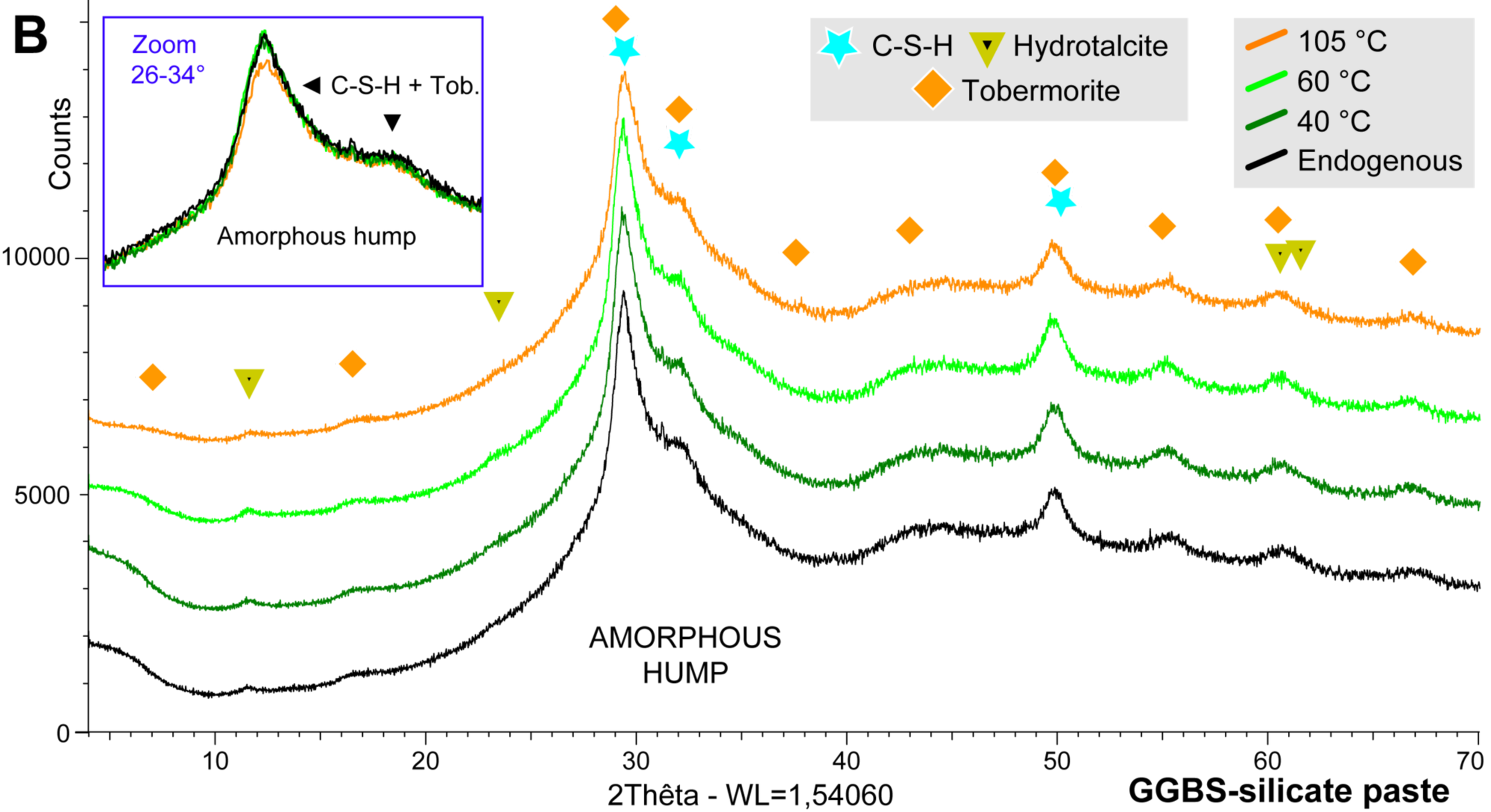
B
Zoom
26-34°
C-S-H + Tob.
Amorphous hump
C-S-H
Hydrotalcite
Tobermorite
105 °C
60 °C
40 °C
Endogenous
Counts
10000
5000
0
AMORPHOUS
HUMP
10
20
30
40
50
60
70
2Thêta - WL=1,54060
GGBS-silicate paste

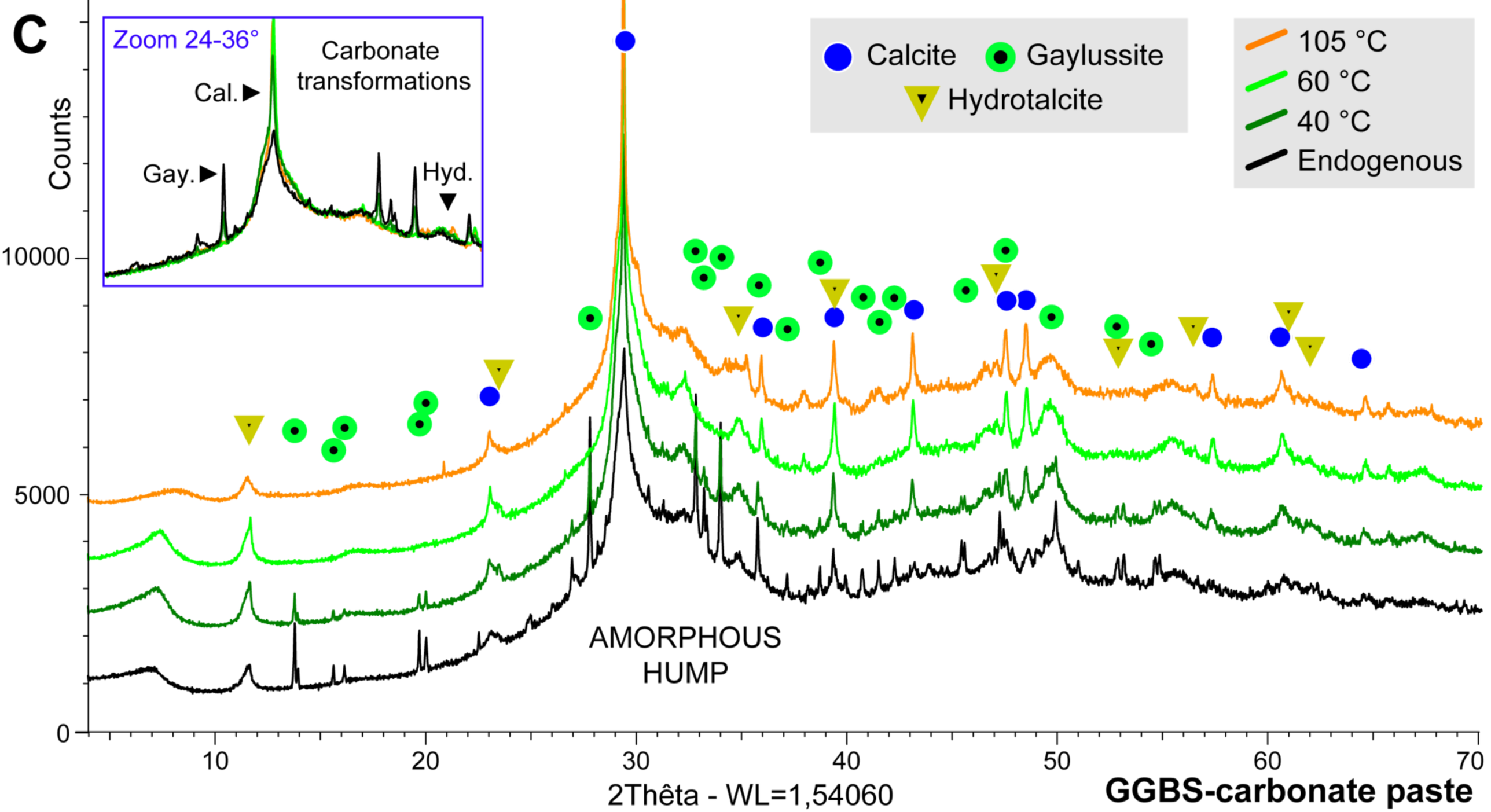
C
Zoom 24-36°
Carbonate transformations
Cal.
Gay.
Hyd.
Counts
Calcite
Gaylussite
Hydrotalcite
105 °C
60 °C
40 °C
Endogenous
AMORPHOUS HUMP
10000
5000
0
10
20
30
40
50
60
70
2Thêta - WL=1,54060
GGBS-carbonate paste

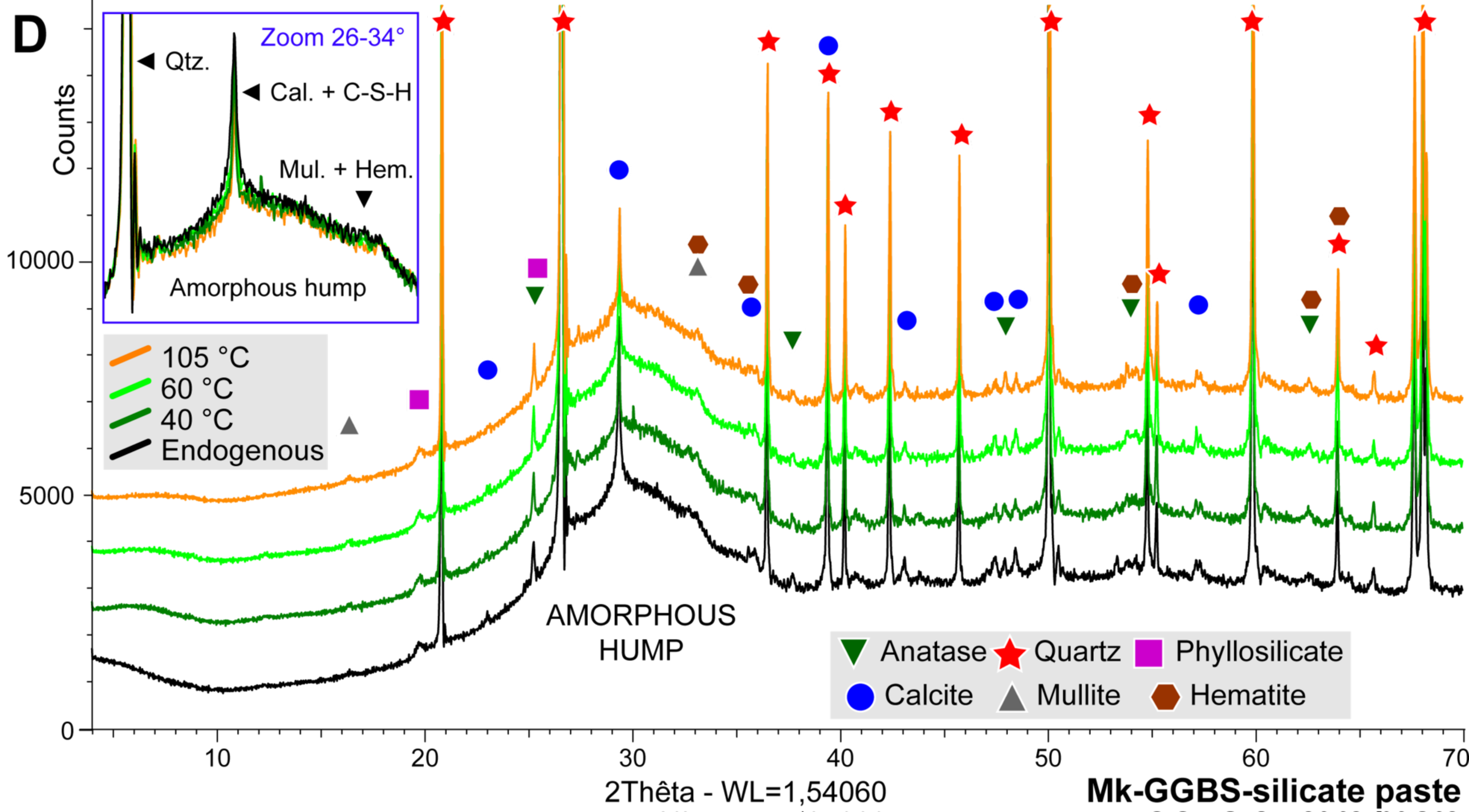
D
Zoom 26-34°
Qtz.
Cal. + C-S-H
Mul. + Hem.
Amorphous hump
Counts
10000
5000
0
105 °C
60 °C
40 °C
Endogenous
AMORPHOUS
HUMP
Anatase
Quartz
Phyllosilicate
Calcite
Mullite
Hematite
10
20
30
40
50
60
70
2Thêta - WL=1,54060
Mk-GGBS-silicate paste

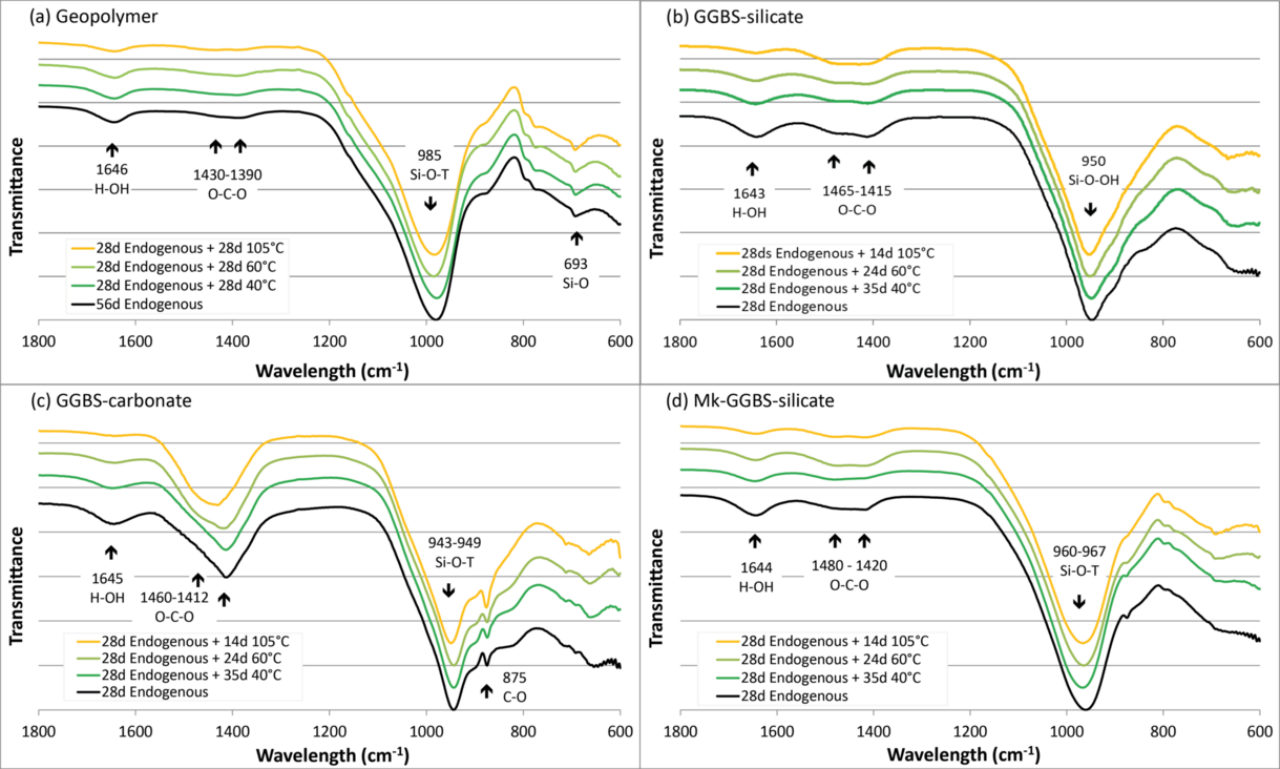
(a) Geopolymer
Transmittance
1646
H-OH
1430-1390
O-C-O
985
Si-O-T
693
Si-O
28d Endogenous + 28d 105°C
28d Endogenous + 28d 60°C
28d Endogenous + 28d 40°C
56d Endogenous
1800
1600
1400
1200
1000
800
600
Wavelength (cm-1)
(b) GGBS-silicate
Transmittance
1643
H-OH
1465-1415
O-C-O
950
Si-O-OH
28ds Endogenous + 14d 105°C
28d Endogenous + 24d 60°C
28d Endogenous + 35d 40°C
28d Endogenous
1800
1600
1400
1200
1000
800
600
Wavelength (cm-1)
(c) GGBS-carbonate
Transmittance
1645
H-OH
1460-1412
O-C-O
943-949
Si-O-T
875
C-O
28d Endogenous + 14d 105°C
28d Endogenous + 24d 60°C
28d Endogenous + 35d 40°C
28d Endogenous
1800
1600
1400
1200
1000
800
600
Wavelength (cm-1)
(d) Mk-GGBS-silicate
Transmittance
1644
H-OH
1480 - 1420
O-C-O
960-967
Si-O-T
28d Endogenous + 14d 105°C
28d Endogenous + 24d 60°C
28d Endogenous + 35d 40°C
28d Endogenous
1800
1600
1400
1200
1000
800
600
Wavelength (cm-1)

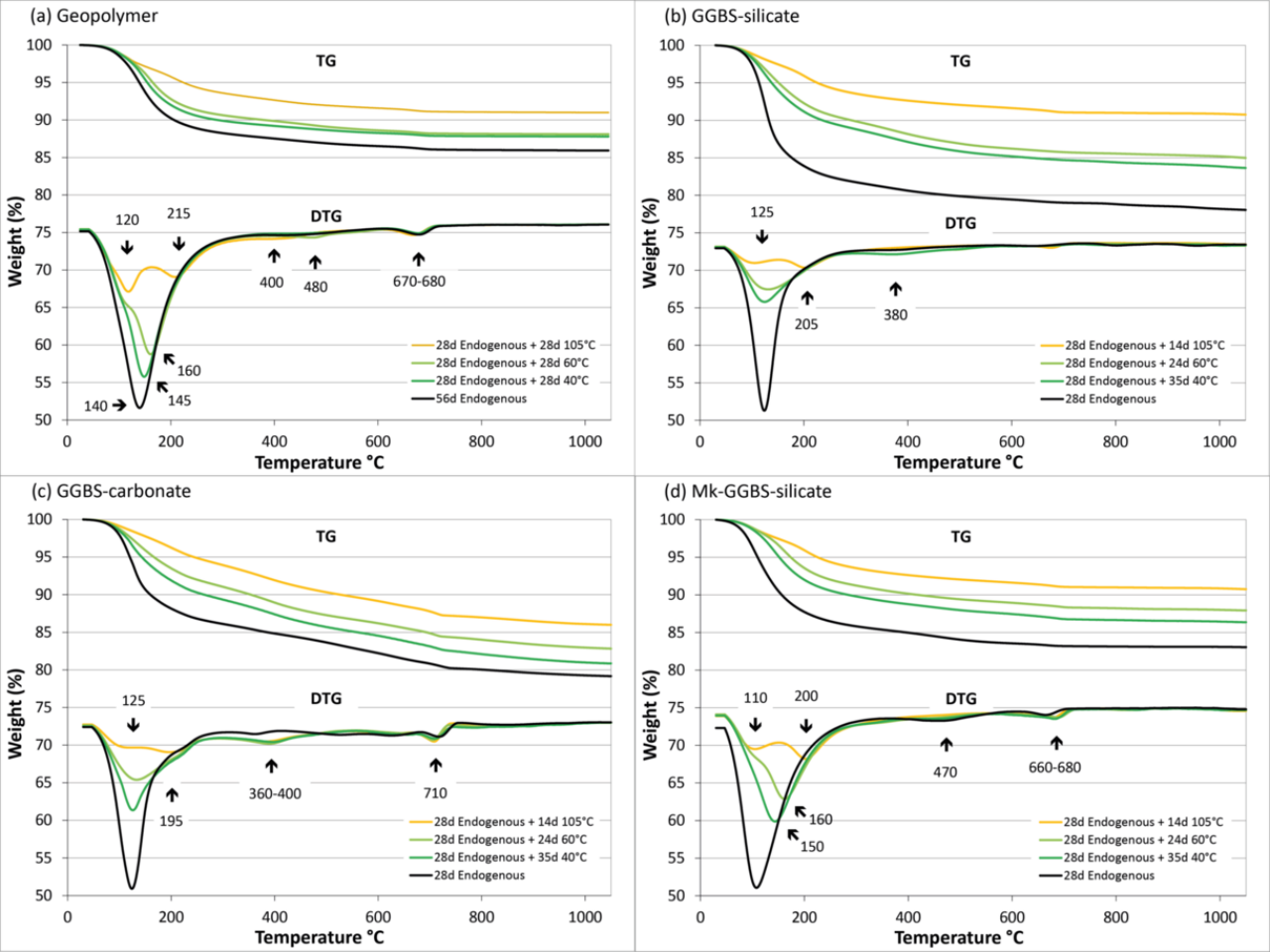
(a) Geopolymer
TG
DTG
Weight (%)
Temperature °C
120
215
400
480
670-680
160
145
140
28d Endogenous + 28d 105°C
28d Endogenous + 28d 60°C
28d Endogenous + 28d 40°C
56d Endogenous
(b) GGBS-silicate
TG
DTG
Weight (%)
Temperature °C
125
205
380
28d Endogenous + 14d 105°C
28d Endogenous + 24d 60°C
28d Endogenous + 35d 40°C
28d Endogenous
(c) GGBS-carbonate
TG
DTG
Weight (%)
Temperature °C
125
195
360-400
710
28d Endogenous + 14d 105°C
28d Endogenous + 24d 60°C
28d Endogenous + 35d 40°C
28d Endogenous
(d) Mk-GGBS-silicate
TG
DTG
Weight (%)
Temperature °C
110
200
470
660-680
160
150
28d Endogenous + 14d 105°C
28d Endogenous + 24d 60°C
28d Endogenous + 35d 40°C
28d Endogenous

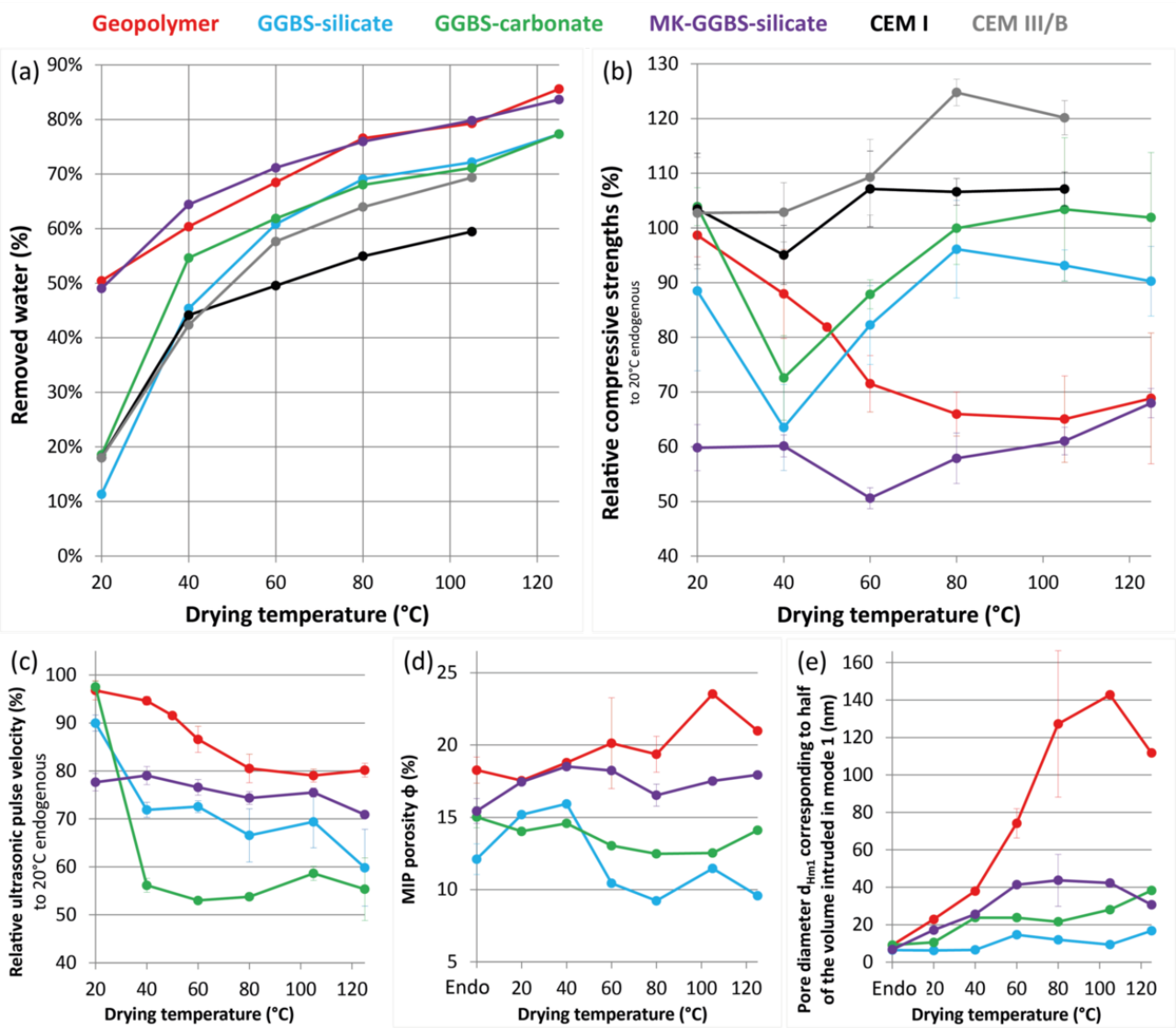
Geopolymer
GGBS-silicate
GGBS-carbonate
MK-GGBS-silicate
CEM I
CEM III/B
(a)
Removed water (%)
Drying temperature (°C)
(b)
Relative compressive strengths (%)
to 20°C endogenous
Drying temperature (°C)
(c)
Relative ultrasonic pulse velocity (%)
to 20°C endogenous
Drying temperature (°C)
(d)
MIP porosity Φ (%)
Endo
Drying temperature (°C)
(e)
Pore diameter d_{Hm1} corresponding to half of the volume intruded in mode 1 (nm)
Endo
Drying temperature (°C)

Raw materials	SiO_2	Al_2O_3	CaO	Fe_2O_3	Na_2O	K_2O	TiO_2	MgO	Mn_2O_3	SO_3	P_2O_5	Cr_2O_3	LOI	Total
CEM I	20.6	4.3	65.5	2.4	0.1	0.2	0.2	0.7	0.1	3.1	0.1	<0.1	2.6	100.0
CEM III/B	30.0	9.5	48.8	2.8	0.5	0.0	0.5	2.7	0.1	2.9	0.2		1.9	100.0
Metakaolin	69.8	22.8	1.2	2.8	0.1	0.3	1.1	0.2	<0.1	<0.1	<0.1	<0.1	1.5	100.0
GGBS	37.5	11.2	42.7	0.4	0.3	0.4	0.7	6.3	0.2	<0.1	<0.1	<0.1	0.0	100.0

Amorphous	47.1 ± 2.5
Quartz	42.3 ± 1.6
Illite	3.5 ± 0.5
Mullite	3.1 ± 0.4
Anatase	1.5 ± 0.1
Calcite	1.0 ± 0.1
Hematite	0.9 ± 0.1
Rutile	0.3 ± 0.1

	Metakaolin	GGBS	CEM I	CEM III/B	Sodium silicate	Sodium carbonate	Water	Sand	W/B	Bulk density
Geopolymer	450.0				354.9		46.2	1350	0.4	2.01
GGBS-silicate		450.0			101.3		141.8	1350	0.4	2.16
GGBS-carbonate		450.0				45.0	198.0	1350	0.4	2.11
Mk-GGBS-silicate	225.0	225.0			228.1		94.0	1350	0.4	2.07
CEM I			450.0				225.0	1350	0.5	-
CEM III/B				450.0			225.0	1350	0.5	-

Condition	Duration	Geopolymer			GGBS-Silicate			GGBS-Carbonate			Mk-GGBS-Silicate		
		ϕ (%)	α (%)	d_{Hm1} (nm)	ϕ (%)	α (%)	d_{Hm1} (nm)	ϕ (%)	α (%)	d_{Hm1} (nm)	ϕ (%)	α (%)	d_{Hm1} (nm)
Autogenous	0d	18.6 ± 1.2	53.2 ± 1.8	9.1 ± 0.6	13.0	71.3	7.1	16 ± 1.1	60.6 ± 1.5	10.2 ± 0.7	17.3	52.8	8.4
	12d	18.1	49.6	9.1									
	14d	18.7	49.8	8.9	14.5	67.7	6.8	15.4 ± 1.5	60 ± 0.4	9.9 ± 2	16.9	52.4	7.2
	16d				14.5	71.1	6.6						
	18±1d	20.7	50.8	9.7				15.7	58.1	9.4	14.8	53.8	7.5
	20d	20.7	50.0	9.4									
	28±1d				11.3	62.5	6.8	15.1 ± 3.2	61.9 ± 0.3	8.9 ± 2.8	16.0	59.4	6.8
	35d	17.6	53.7	9.5	13.8 ± 2.3	68.6 ± 5	6.4 ± 0.3	15.2	62.4	9.6	14.9	53.3	6.8
	48±1d	16.7	48.3	8.6	10.1	66.2	6.6	14.4	59.7	7.6	14.3	57.6	6.8
	52d	18.8	56.0	9									
	60±1d	16.5	48.5	8.7	10.6 ± 1	62.2 ± 2	6.5 ± 0.3	13.9	60.6	9.1	13.8	54.3	5.7
	158±11d	16.1	52.1	9	12.0	63.4	5.9	13.0	60.3	7.7	15.5	47.5	5.0
125°C	13±1d	21.0	44.5	111.8	9.6	58.0	16.8	14.1	66.1	38.3	17.9	46.5	30.7
105°C	14d	23.5	47.0	142.8	11.5	65.4	7.5	12.5	59.4	28.1	17.5	44.6	42.3
	58d							13.7	68.8	29.8			
80°C	18±2d	19.4 ± 1.2	46.7 ± 2	127.3 ± 39.1	9.2	59.2	12.0	12.5	63.0	21.6	16.5 ± 0.8	55.5 ± 2.5	43.8 ± 13.8
	58±1d	19.8 ± 2.1	46.7 ± 1.2	143.3 ± 0.1				12.5	74.0	28.4			
60°C	20d	20.1 ± 3.1	45 ± 1.6	74.2 ± 7.8									
	28d				10.4	55.1	14.7	13.0	64.2	23.8	18.2	46.5	41.4
	59d	18.7	44.7	87.9	10.0	60.3	18.4	12.5	72.2	24.2			
40°C	34±1d	18.8	48.7	38	15.9	51.0	6.6	14.6	57.5	23.8	18.5	50.5	25.6
	59d	17.5	46.6	37.5	12.0	51.4	13.5	14.1	68.0	32.3	17.0	51.5	32.4
20°C-50%RH	49d	17.5	47.8	22.9	15.2	61.0	6.3	14.0	59.8	10.6	17.5	51.7	17.2
	59d	17.3 ± 0.2	49.3 ± 1.1	22.8 ± 3				14.4	58.5	6.8			
Vacuum	60d	17.0	49.5	12.1	12.7 ± 1	59.9 ± 4	5.9 ± 0.2						
20°C 95%RH	59d							13.9	59.4	8.0			
	70d	19.0	53.3	8.7	11.6	73.4	5.9						

<table>
<tr><th>Drying condition</th><th>Geopolymer</th><th>GGBS-silicate</th><th>GGBS-carbonate</th><th>Mk-GGBS-silicate</th></tr>
<tr><td>20°C
50%RH</td><td rowspan="2">Slow (2-4 weeks), efficient (50-60%) drying; no strength damage; porosity little changed; no mineralogical transformation</td><td>Very slow (>2 months), inefficient (<25%) drying; no strength damage; porosity not changed; no mineralogical transformation</td><td>Very slow (>2 months), inefficient (<30%) drying; no strength damage; porosity not changed; no mineralogical transformation</td><td rowspan="2">Slow (2-3 weeks), efficient (50-67%) drying; strength damage; porosity changed; mineralogical transformations</td></tr>
<tr><td>40°C
(low RH)</td><td rowspan="2">Slow (2-4 weeks), efficient (50-67%) drying; strength damage; porosity little changed; no mineralogical transformation</td><td rowspan="2">Slow (1-4 weeks), efficient (60-67%) drying; strength damage; porosity little changed; mineralogical transformations</td></tr>
<tr><td>60°C</td><td rowspan="4">Fast (<1 week), efficient (65-85%) drying; strength damage; pore size changed significantly; no mineralogical transformation</td><td rowspan="4">Fast (<1 week), efficient (65-85%) drying; strength damage; pore size changed significantly; mineralogical transformations</td></tr>
<tr><td>80°C</td><td rowspan="3">Fast (<1 week), efficient (70-80%) drying; no strength damage; pore size little changed; no mineralogical transformation</td><td rowspan="3">Fast (<1 week), efficient (70-80%) drying; no strength damage; pore size little changed; mineralogical transformations</td></tr>
<tr><td>105°C</td></tr>
<tr><td>125°C</td></tr>
</table>